Large eddy simulation of atmospheric boundary layer flow over a realistic urban surface

Dissertation

submitted to and approved by the

Department of Architecture, Civil Engineering and Environmental Sciences
University of Braunschweig – Institute of Technology

and the
Department of Civil and Environmental Engineering
University of Florence

in candidacy for the degree of
Doktor-Ingenieur (Dr.-Ing.) / Dottore di Ricerca in
Processes, Materials and Constructions in Civil and Environmental Engineering and for the Protection of the Historic-Monumental Heritage

by
Marco Giovanni Giometto
born 03/04/1985
from Sandrigo (VI), Italy

Submitted on	16/09/2014
Oral examination on	07/11/2014
Professorial advisors	Prof. Anna Saetta Prof. Manfred Krafczyk

2016

Acknowledgements

First of all, I am greatful to my thesis directors, Prof. Anna Saetta and Prof. Manfred Krafczyk, for they supervised my research and provided support during these years of academic research, giving me the opportunity to learn new topics in applied mathematics and fluid mechanics, and to visit several research laboratories throughout Europe, which significantly contributed to the growth of my education.

I express my gratitude to the two coordinators of the Doctoral School, Prof. Claudio Borri and Prof. Klaus Thiele. They are the "columns" of the international doctoral course, and I am very grateful for they allowed me to enjoy such a stimulating environment.

A special acknoledgement goes to Prof. Marc Parlange and to the EFLUM group at the École Polytechnique Fédérale de Lausanne. They gave me unique opportunities to grow my knowledge and walked me through the fascinating topic of environmental fluid mechanics and turbulence.

Further, I warmly acknowledge Prof. Andreas Christen from the Geography department at UBC, for sharing his great knowledge and sincere passion for urban

meteorology, for his constant guide throughout this work and for his kindness, which facilitated a fruitful collaboration.

Another warm thank-you goes to Prof. Mario Putti from the department of Applied Mathematics at Padua University, for his availability, capacity of synthesis, and for his attempt to provide me with some of his mathematical rigor.

I acknowledge the EPFL high performance computing (HPC) center and the Swiss National supercomputing center (CSCS) for the use of their clusters and for providing excellent support during these years.

I am very thankful to my friends and colleagues Diego, Giuseppe, Laura and Stefano, for their precious advices, for their kindness and irony.

I thank all my friends and colleagues of the International Phd program, with whom I shared stimulating discussions and wonderful moments throughout these years, in particular: Alberto, Giuseppe, Lucia, Pietro, Simona, and Vincenzo.

Last but not least, a big thank-you goes to my parents, for the great support and care throughout these years.

Abstract

Most of our current knowledge on flow and turbulence in realistic urban roughness sublayers (RSL) originates from sporadic campaigns with single-point measurements from towers in cities. Such measurements are not able to properly quantify the impact of terms such as dispersive momentum fluxes, wake production, dispersive transport and dissipation of turbulent kinetic energy (TKE). Further, we assume that single-point measurements are representative if used as surrogate for horizontally-averaged quantities over the entire urban domain.

To quantify the relevance of non-measurable terms and explore the spatial variability of the flow field in generating, transporting and dissipating TKE, a series of Large Eddy Simulations (LES) is performed to characterize the airflow over and within a truthful building-resolving urban geometry in the city of Basel, Switzerland. The extend of a representative subset for the city is first identified, based on the convergence of averaged flow statistics. Further, a 512 $\times$ 512 m wide domain is chosen to be centered around a tower where single-point turbulence measurements at six heights are available. To account for variability connected to the closure model, two values of the

surface hydrodynamic roughness length z_0 and two LES closure models are considered: the Static and the Lagrangian scale-dependent Smagorinsky models. Buildings are represented through a discrete-forcing immersed boundary method (IBM) and based on detailed real geometries from a surveying dataset.

The local model output at the tower location compares well against measured data for two chosen approaching angles of the flow, confirming LES in conjunction with IBM a valuable tool to study turbulence and dispersion within a real urban RSL. The simulations confirm that mean velocity profiles in the RSL are characterized by an inflection point z_γ, located above the average building's height z_h. TKE in the RSL is primarily produced above z_γ, and turbulence is transported down into the urban canopy layer (UCL, i.e. street canyons, backyards). Pressure transport is found to be significant in the very near wall regions. Further, spatial variations of time-averaged variables and non-measurable dispersive terms are important in the urban RSL above a real urban surface and should therefore be considered in future urban canopy parameterization developments.

Contents

List of Figures

List of Tables

CHAPTER 1

Introduction

1.1 Turbulence modeling for urban applications

The problem of urban development and its impact on the environment and safety/health of citizens have been challenging tasks for policy-makers: a correct understanding of the urban dynamics and its interaction with the surrounding rural areas is of fundamental importance in view of increasing urbanisation and consequent demand for infrastructures.

A correct modeling of flow and turbulence in the urban roughness sublayer (RSL) – the atmospheric layer from ground to 2 to 5 times the average builing's height z_h – is essential to properly predict weather, air quality, and dispersion of gases in urban environments. Within the RSL, flow and turbulence exhibit strong spatial variations in both the vertical and the horizontal directions. This is caused by the flow around the local configuration of roughness elements (buildings and trees). Hence,

one-dimensional surface scalings relying on horizontal homogeneity such as Monin-Obukhov similarity (MOST) are not applicable in the RSL (Rotach, 1999; Roth, 2000). MOST is strictly applicable only in the inertial sublayer (ISL), whose existence in urban environments is subject to debate (Jimenez, 2004). Consequently three-dimensional approaches such as computational fluid dynamics (CFD) are required to properly describe flow, turbulence and exchange in the RSL.

However, for many applications, building-resolving information is neither required nor are CFD approaches computationally feasible. In mesoscale weather forecasting and air pollution dispersion models, urban canopy parameterizations (UCP) are used to represent the effects of urban surfaces. UCPs rely usually on a horizontally averaged approach, where the RSL is represented as a 1D column, often for simplified geometries such as infinite street canyons or cubical blocks of buildings. The vast majority of UCPs use MOST relationships to compute vertical fluxes of momentum and scalars such as heat, humidity or pollutants between the urban facets and the atmosphere, irrespective of the problem outlined above (Grimmond et al., 2010).

Proper techniques to reinstall a 1D approach in a truly three-dimensional RSL should account for the inherently variable canopy morphology, and its hierarchical structure of scales (from the street or canyon scale to the regional scale) as discussed in Britter and Hanna (2003). For instance, in the horizontal averaging process of RANS equations, additional terms arise in the time-averaged momentum balance, called *dispersive fluxes* (Raupach and Shaw, 1982), which physically represent spatial correlations between mean vertical flow around buildings and the time-averaged quantity exchanged. The very few modeling studies directly determining dispersive fluxes by means of CFD have shown that these terms can be highly relevant, in addition to Reynolds stress, to the overall momentum transfer in the RSL over rigid canopies (Coceal et al., 2006; Martilli and Santiago, 2007).

On a fundamental perspective, efforts have been devoted using experimental and numerical approaches to study RSL dynamics and scalings over simplified urban-like

surfaces, mostly in the form of staggered/aligned cubical arrays (Cheng and Castro, 2002; Coceal et al., 2006; Xie and Castro, 2006). The few characteristic length scales that characterize roughness elements in such arrays provide a setting that eases simulation, analysis and theory-development. The approach is justified on the grounds that one should first understand flow over rough surfaces in its simplest form, before introducing complexities such as variable roughness height or shapes, which would result in a broader spectra of scales and dynamics. However, flow over cubes might be difficult to compare with the flow over real urban canopies, where the additional set of length scales, connected to the intrinsic heterogeneity of the surface, might completely modify the dynamics of the system. For instance, boundary layer flow over surface mounted cubes with variable element heights, studied in Cheng and Castro (2002) report a thinner ISL when compared with uniform height settings, suggesting an ISL region might not even exist in certain realistic urban canopies.

In the past decades experimentalists have devoted significant efforts to measure the relevant processes that drive mean flow and turbulence in the RSL over real cities (Christen et al., 2009, 2007; Eliasson et al., 2006; Grimmond and Oke, 1999; Peng and Sun, 2014; Ramamurthy et al., 2007). However, such experimental field-studies are limited to measurements at a few points and cannot capture the full three-dimensional flow field in its heterogeneous state. The lack of homogeneity in the statistical properties of the flow within the RSL may question the usage of point measurements as a surrogate of horizontally averaged quantities, as proposed by Rotach (1993a,b) and Christen et al. (2009).

The strong spatial variability of the flow represents in fact the main challenge preventing the development of a comprehensive physically-based theory for the vertical structure of the RSL, such as the classic Monin-Obukhov similarity theory (MOST) (Monin and Obukhov, 1954) for the idealized surface layer. (the validity of MOST for boundary layer flow over heterogeneous surfaces with periodic patterns has been investigated in Bou-Zeid (2004)).

The increased availability of high resolution digital datasets on urban morphology (e.g. high resolution LiDAR scans, vectorial models based on surveyed data, etc.) is recently promoting the use of real topographies in numerical studies (see for instance Kanda et al. (2013)). Further, advances in computational power now allows to represent the three-dimensional processes of interest at the neighborhood scale ($10^2 - 10^3$ m). This is is at least relaxing constraints with regard to the feasibility and costs of numerical simulations over real urban morphometries.

Output from numerical models, such as Large Eddy Simulations (LES), can therefore be used to understand the physics of the flow and quantify the most relevant terms and processes that occur in relistic urban RSLs. This is the goal of the current study. Here LES is used to resolve the airflow over and within a truthful urban geometry to (1) spatially characterize mean flow and turbulence in the RSL, (2) to determine the role of non-measurable terms such as dispersive momentum fluxes, wake production, dispersive transport, pressure transport, dissipation of TKE, and (3) to determine how representative are single-point measurements, when used as surrogate for horizontally-averaged quantities over the entire urban domain. Such informations can then be used in order to guide and validate current upscaling for one-dimensional UCPs.

The main concepts regarding the atmospheric boundary layer and its approximation in simulations are briefly reviewed in chapter 2. Chapter 3 describes the numerical algorithm, the site and instrumentation, the processing of the tower data, and provides informations on the digital surface model. Chapter 4 proposes a sensitivity analysis to determine the geometrical requirements for comparison with measured data, and a representative subset for the urban surface is identified. The structure of mean flow and turbulence in the RSL for the considered subset of the city is proposed in Chapters 5 and 6. Chapter 5 focuses on first and second order statistics and on their comparison against tower measurements, whereas Chapter 6 presents a detailed analysis of TKE budget terms in the RSL.

Throughout the study we will alternate the Einstein summation notation, where

x, y, z will denote the stream-wise, span-wise and vertical coordinates with the vector notation, based on convenience. The boundary layer height will be denoted as δ whereas a given height in the domain will be denoted as z_{label}. Further, $\widetilde{(\cdot)}$ is used to denote a spatially filtered variable (implicit LES filter). $\overline{(\cdot)}$ denotes time-averaging or ensemble averaging (depending on the context), $\langle\cdot\rangle$ denotes horizontal (x, y) averaging, time fluctuations are written as $(\cdot)'$ (therefore $\overline{(\cdot)'} = 0$) and departures of time-averaged terms with respect to their horizontal mean are denoted as $\overline{(\cdot)}''$ (therefore $\langle\overline{(\cdot)}''\rangle = 0$). $(\cdot)^*$ will be used to denote a normalized variable.

CHAPTER 2

Numerical modelling of atmospheric boundary layer flows

2.1 The atmospheric boundary layer

This sections aims at providing a short introduction on the concept of atmospheric boundary layer, which sets the the basis for later discussion. The troposphere can be divided in two layers (see fig. 2.1), the atmospheric boundary layer (ABL), that layer where we all live and which is in direct contact with the surface, and the – loosely defined – free atmosphere (FA), which is the remainder of the air and is usually in a laminar state. The atmospheric boundary layer responds to surface forcing within time scales of $\sim 1h$ (Stull, 1988) and is characterized by the presence of turbulent motions in the flow, which is probably the most fascinating feature of it, and which manifests itself in a broad range of irregular swirls of motion called eddies. Typical forcing include frictional drag, evaporation and transpiration, heat transfer, pollutant emission, and terrain induced flow modification. It's height (δ) can vary quite wildly

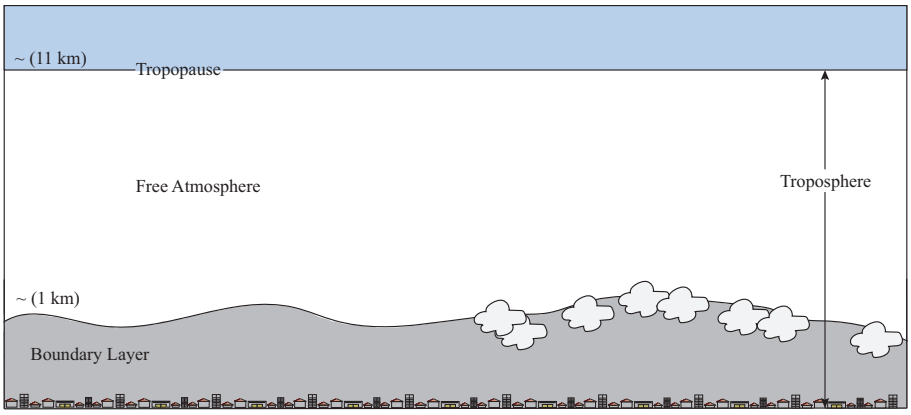

Figure 2.1: Layers composing the troposphere.

from few meters under extremely stably stratified environments up to $\sim 3km$ during daytime, depending on the geographical location. The ABL structure has a natural daily evolution cycle, which spans a broad spectra of dynamical/thermodynamical regimes. The three major components of this structure are the stable boundary layer (SBL), the mixed layer (ML) and the residual layer (RL). Is then common to define an additional layer, which is present irrespectively of the specific regime, namely the *surface layer* (SL), which is identified as that region near the surface where turbulent fluxes and stress vary by less than 10% in magnitude. The boundary layer is characterized by a potentially stable stratification at nighttime (SBL), mainly due to radiative cooling, during which turbulence is weak and intermittent, and the flow is populated by Kelvin-Helmoltz instabilities and meandering motions. With the onset of the day the heat transfer from the warm surface, together with the radiative cooling from the clouds' top generates thermals and the resulting intense turbulent activity tends to well mix scalars (heat, moisture) and momentum in the vertical, building up the ML. Virtual potential temperature profiles in this regime, for instance, are nearly adiabatic in the middle portion of the boundary layer, whereas a superadiabatic layer is usually present at the surface location. A stable layer at the top of the ML acts as a lid to the rising

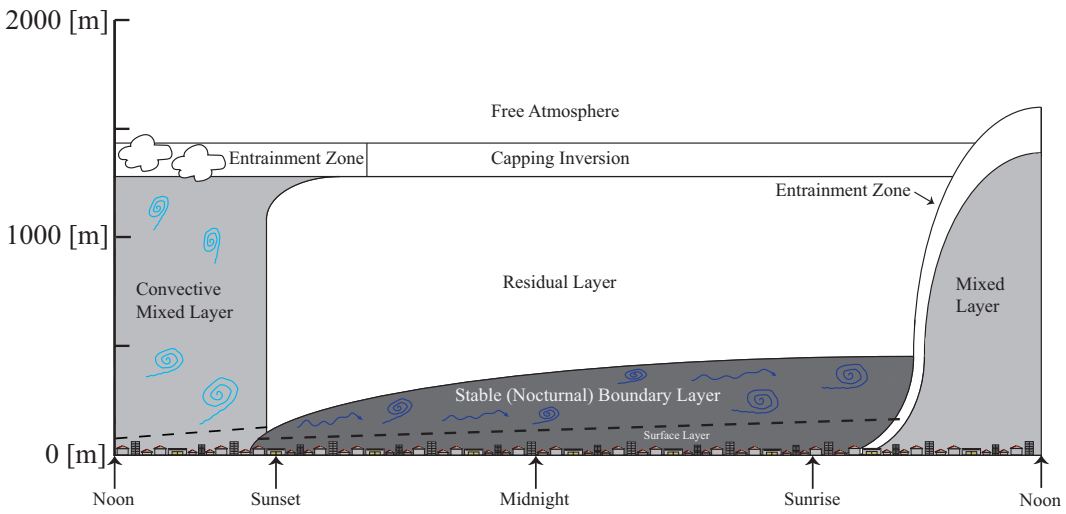

Figure 2.2: Redrawn based on (Stull, 1988). Typical boundary layer evolution cycle. The very turbulent 'mixed layer' (ML), followed by a turbulence decay period usually referred to as 'residual layer' (RL), and ultimately the 'stable boundary layer' (SBL).

thermals, separating the laminar FA from the turbulent ML. Air is entrained in this region (often referred to as *entrainment zone*) from the FA above, causing a growth of of ML, which reaches is maximum depth in the late afternoon. Little before sunset the thermal forcing ceases, resulting in a relatively long turbulence decay period and formation of the RL (Stull, 1988). Further, in urban meteorology it's then customary to subdivide the surface layer, as displayed in fig. 2.3, to account for different forcing (dynamical and thermodynamical) mechanisms and statistical properties characterizing the flow. The concept of urban canopy layer (UCL) is introduced to denote that layer where people live in a city, which is usually bounded by the mean height of the roofs z_h, and where mean flow and turbulence are highly dependent on the actual configuration of the obstacles relative to the mean wind. The roughness sublayer (RSL) follows, as we move up high in the atmosphere, to denote a layer where the effects of isolated roughness elements are still present (usually between 3 and 5 times the mean building

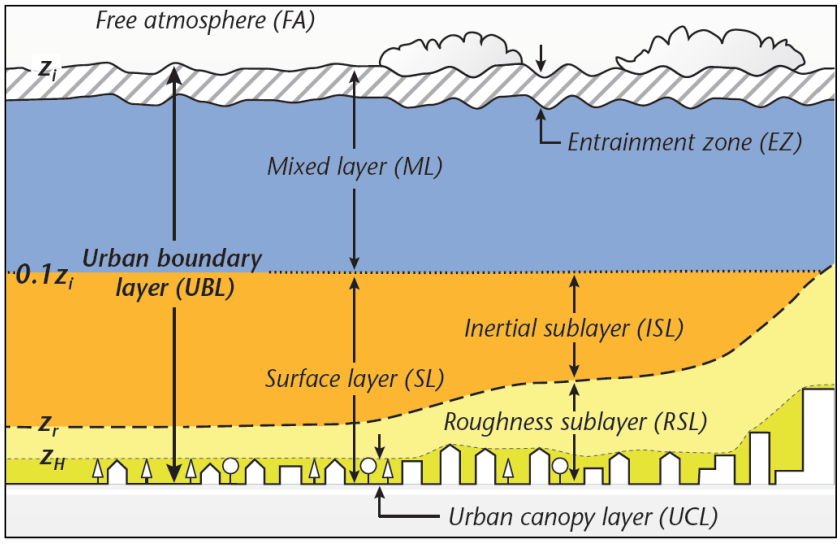

Figure 2.3: Layering of the urban boundary layer structure. Reproduced from lecture slides of class GEOB401 at the University of British Columbia - Vancouver (Prof. Andreas Christen).

height z_h). Turbulence statistics in the RSL are heterogeneous in space, depend on the surface features, and share similarities with flow over vegetation canopies, which are patterned on a plane mixing layer (Raupach et al., 1996) due to the instabilities associated with the characteristic strong inflection in the mean velocity profile. The so-called inertial sublayer (ISL) separates then the RSL from the outer regions of the boundary layer and is characterized by homogeneous turbulence, constant momentum flux profiles, and statistics that are only a function of a characteristic velocity scale u_τ and of the height from the surface z.

2.2 Universal scaling in the atmospheric boundary layer

Geophysical flows fall in the general category of wall bounded flow over fully rough surfaces, being characterized by a roughness Reynolds number $k_s^+ = \frac{k_s u_\tau}{\nu} \gg 1$, where k_s is the so-called 'equivalent' or 'effective' sand roughness. k_s^+ is typically so high that the buffer-layer viscous cycle is completely destroyed and the flow becomes independent from viscosity, being most of the drag generated by pressure on the roughness elements (form drag). Under neutral conditions, such flows are governed by two sets of parameters. In the near wall regions (RSL) the only relevant parameters are the friction velocity $u_\tau = \sqrt{\tau_w/\rho}$ and k_s, where τ_w is the stress that the turbulent flow is exerting at the wall. At a given distance from the wall the coherent structures populating the boundary layer are limited by δ, which therefore becomes the relevant length scale in the so-called outer layer. If δ/k_s is large enough, between the outer region and the RSL there is an overlap layer, the so-called inertial sublayer (ISL), in which the only relevant scales are the distance from the wall z and the friction velocity u_τ, leading to the well known equilibrium log profile (Nikuradse, 1950):

$$U^+(z) = \kappa^{-1} \log\left((z-d)/k_s\right) + 8.5 + \Pi\kappa^{-1} W(z/\delta), \tag{2.1}$$

Where the Von Karman constant, $\kappa \approx 0.4$, depends only on the properties of the ISL and is believed to be universal, d is the displacement height and $W(z/\delta)$ is the so called wake function, and account for contributions of outer-layer dynamics (Pope, 2000). The shift d from some reference location is usually determined empirically to maximize the quality of the logarithmic fit in equation 2.1, and is typically some fraction of k (Raupach et al., 1991). The wake function it's typically negligible below $z/\delta \approx 0.15$ (upper limit of the logarithmic layer), and for zero pressure gradients the pre-factor Π is of order 1. An alternative formulation of the equilibrium logarithmic

law, which is the preferred one in the geophysical community reads:

$$U^+(z) = \kappa^{-1} \log\left((z-d)/z_0\right) + \Pi\kappa^{-1} W(z/\delta), \tag{2.2}$$

where $z_0 = 0.033 k_s$ is the so-called hydrodynamic roughness length. If k_s is a significant fraction of δ then the roughness modifies the whole boundary layer, and the logarithmic profile might not survive (Jimenez, 2004). The ratio δ/k_s is large in open rural areas, but not necessarily so over cities or forests (Cheng and Castro, 2002), given that the RSL may extend to a significant height, the inertial sublayer (ISL) then becomes squeezed between the RSL and the outer layer.

2.3 The Large Eddy Simulation (LES) approach

From the point of view of simulations the problem is mainly computational cost. In simulations of atmospheric flow over an urban canopy, to be reasonably free from direct roughness effects a vertical extend of about $\delta/k \gtrapprox 50$ is required (Jimenez, 2004). Assuming the urban canopy has an average height of 10 m we have $k^+ \approx 10^6$ and to have a well-defined rough turbulent flow we therefore need $\delta^+ = \delta/k \cdot k^+ = \delta u_\tau/\nu \gtrapprox 5 \cdot 10^7$. The largest direct numerical simulations (DNS) of wall-bounded flows at present are characterized by $\delta^+ \approx 4000$. The majority of scales in turbulent flows are in the dissipative range, but most of the of momentum/scalar transport is caused by the energy-containing scales of turbulence. This consideration has motivated the development of approaches that reduce the resolution requirements in the dissipative range, and LES falls into this category of parameterizations. In LES only the energy-containing motions are resolved and the effects of the unresolved modes are modeled (Pope, 2000). There are four conceptual steps in LES:

- A filtering operation is defined to decompose the velocity $u_i(\mathbf{x},t)$ into the sum of a filtered (resolved) component $\tilde{u}_i(\mathbf{x},t)$ and a residual (or subgrid-scale, SGS)

model	acronym	Resolution
Direct numerical simulation	DNS	All scales of turbulence are fully resolved
Large-eddy simulation with near wall resolution	LES-NWR	The filter and grid are sufficiently fine to resolve 80% of the energy everywhere
Large-eddy simulation with near-wall modelling	LES-NWM	The filter and grid are sufficiently fine to resolve 80% of the energy remote from the wall but not in the near-wall region.
Very-large-eddy simulation	VLES	The filter and grid are too coarse to resolve 80% of the energy

Table 2.1: Resolution in DNS and in some variants of LES. Reproduced from Pope (2000).

component $u_i'(\mathbf{x},t)$. The filtered velocity field $\tilde{u}_i$ represents the motion of the large eddies;

- the equations for the evolution of the filtered velocity field are derived from the Navier-Stokes equations. These equations are of the standard form, with the momentum equation containing the residual SGS stress tensor that arises from the residual motions;

- closure is obtained by modeling the residual stress tensor most simply by an eddy viscosity model;

- the model filtered equations are solved numerically for $\tilde{u}_i$, which provides an approximation to the large-scale motions in one realization of the turbulent flow.

The equations for the filtered $\tilde{u}_i$ are unclosed and closure is achieved by modelling the residual (or SGS) stress tensor τ_{ij}^{sgs}. The filtered velocity field depends on the type of filter and the filter width Δ, yet these quantities usually do not appear directly in the equations, they appear only indirectly through the model for τ_{ij}^{sgs}. Explicit SGS models do exist, where the filtering operation is performed on the equations after the discretization process, but this comes at high price (it's roughly an order of magnitude more expensive from a computational point of view).

There are some distinctions among variants of LES which are summarized in table 2.1. Considering the flow remote from walls it's possible to make a distinction between LES and VLES: in LES the filtered velocity field accounts for the bulk (say 80%) of the turbulent kinetic energy everywhere in the flow field. In VLES the grid and filter are too large to resolve the energy containing motions, and instead a substantial fraction of the energy resides in the residual motions. VLES can be performed on coarser grids and is less expensive but the simulations is more strongly dependent on the modelling of the residual motions. In practice the fraction of energy resolved is seldom estimated so that it is not clear whether a particular simulation is LES or VLES (Pope, 2000).

CHAPTER 3

Materials and Methods

3.1 Numerical algorithm

3.1.1 Equations and discretization

We solve the isothermal filtered Navier-Stokes equations in their rotational form (Orszag and Pao, 1975), to ensure conservation of mass and kinetic energy:

$$\begin{cases} \frac{\partial \tilde{u}_i}{\partial t} + \tilde{u}_j(\frac{\partial \tilde{u}_i}{\partial x_j} - \frac{\partial \tilde{u}_j}{\partial x_i}) = -\frac{\partial \tilde{\pi}}{\partial x_i} + \frac{\partial \tau_{ij}^{SGS}}{\partial x_j} - \frac{1}{\rho}\frac{\partial \tilde{p}_\infty}{\partial x_i}\delta_{i1} + \tilde{f}_i\delta(x_i - x_i^{\Gamma_b}) & \text{in } \Omega \times [0,T], \\ \frac{\partial \tilde{u}_i}{\partial x_i} = 0 & \text{in } \Omega \times [0,T], \\ \frac{\partial \tilde{u}}{\partial z} = \frac{\partial \tilde{v}}{\partial z} = 0, \quad \tilde{w} = 0, & \text{in } \Gamma_{\text{top}} \times [0,T], \\ (\tilde{\mathbf{u}} \cdot \tilde{\mathbf{n}})\tilde{\mathbf{n}} = \tilde{\mathbf{u}}_N = 0 & \text{in } \Gamma_b \times [0,T], \\ \tau_w = (\kappa \|\tilde{\mathbf{u}} - \tilde{\mathbf{u}}_N\|_2 / \ln[1 + \Delta/z_0])^2 & \text{in } \Gamma_b \times [0,T]. \end{cases} \tag{3.1}$$

where $\tilde{u}_i$ are the filtered velocity components in the three coordinate directions, $\tilde{\pi}$ is a modified filtered pressure field, namely $\tilde{\pi} = \frac{\tilde{p}}{\rho} + \frac{1}{3}\tau_{ij}^{SGS} + \frac{1}{2}\tilde{u}_i\tilde{u}_i$, ρ is a reference density, and τ_{ij}^{SGS} represent the subgrid terms, which arise from the filtering operation (Pope, 2000), $\frac{1}{\rho}\frac{\partial \tilde{p}_\infty}{\partial x_i}$ is a volumetric forcing term which is introduced to drive the flow, and $\tilde{f}_i$ is a forcing term that is used to impose the desired boundary condition at the surface location, it has a finite value at the buildings interface (Γ_b) and is zero elsewhere. $\tilde{\mathbf{u}}_N$ is the normal-to-surface velocity vector, $\Delta = (dx \times dy \times dz)^{1/3}$ and z_0 is the hydrodynamic roughness length for the considered surface. The argument of the log function in Eq. 3.1 has been regularized by adding a unitary constant (Chester et al., 2007). Atmospheric stratification is not accounted for in the present study, and viscous contributions are also neglected, given the high Reynolds number characterizing the problem. The LES algorithm has been previously used to study land atmosphere interaction processes (Albertson and Parlange, 1999a,c) and to develop and test linear and non-linear LES subgrid-scale models (Bou-Zeid et al., 2005; Lu and Porté-Agel, 2010, 2013; Meneveau et al., 1996; Porté-Agel, 2004). Equations are solved in strong form on a regular domain Ω, a pseudospectral collocation approach (Orszag, 1969a, 1970) based on truncated Fourier expansions is used in the x, y coordinate directions, whereas a second-order accurate centered finite differences scheme is adopted in the vertical direction, requiring a staggered grid approach for the $\tilde{u}, \tilde{v}, \tilde{p}$ state variables (these are stored at $[j+1/2]\Delta z$, with $j = 1, N_z$). Time integration is performed adopting a fully explicit second-order accurate Adams-Bashforth scheme. A fractional step method (Chorin, 1968; Kim and Moin, 1985) is adopted to compute (in a decoupled fashion) the pressure field by solving an additional Poisson equation, which is derived enforcing mass continuity for the incompressible fluid $\frac{\partial \tilde{u}_i}{\partial x_i} = 0$. All nonlinear terms are dealiased adopting a $3/2$ rule (Canuto et al., 2006), to avoid piling up of energy in the high wavenumber range (Kravchenko and Moin, 1997). In the following we will provide additional details on the numerical procedure.

3.1.2 Numerical discretization

The mixed approach in space (pseudospectral / finite differences) is justified on the basis that our boundary conditions are periodic in the horizontal directions, whereas non-periodic in the vertical direction. To achieve spectral accuracy in the vertical direction one could rely on Chebyshev polynomials, which also admit a fast transform (Canuto et al., 2006). However, the main drawback of Chebyshev polynomials is that the mesh spacing becomes exceedingly small at the boundaries, posing serious constraints on the Courant-Friedrichs-Lewy (CFL) condition. Further, a semi-implicit approach, even considering preconditioning (Canuto et al., 2006), is overly expensive, given that in LES simulations it's important to maintain a low CFL to avoid time-filtering of the solution.

For the collocation method we require that the strong form of Eq. 3.1 be satisfied at the grid points. Considering the set of collocation nodes

$$x_j = \frac{2\pi j}{N_x}, \quad j = 0, 1, \ldots, N_x - 1, \tag{3.2}$$

$$y_j = \frac{2\pi j}{N_y}, \quad j = 0, 1, \ldots, N_y - 1, \tag{3.3}$$

$$z_j = \frac{2\pi j}{N_z}, \quad j = 0, 1, \ldots, N_z - 1, \tag{3.4}$$

the pseudospectral collocation approach approximates a given variable θ in terms of its discrete Fourier series

$$\theta_N(x,y,z) = \sum_{k_x} \sum_{k_y} \hat{\theta}(k_x, k_y, z) \exp\left(i[k_x x + k_y y]\right), \tag{3.5}$$

where $\hat{\theta}(k_x, k_y, z)$ is the complex Fourier coefficient associated with the approximation θ_N of θ, $-N_x/2 \leq k_x \leq N_x/2 - 1$ and $-N_y/2 \leq k_y \leq N_y/2 - 1$ are the wavenumbers in the x, y directions. $\hat{\theta}(k_x, k_y, z)$ is computed through the FFT algorithm, which

is characterized by an operation count of roughly $3N\log 2N$. Differentiation in the horizontal direction x,y is based upon the values of the function u at the collocation nodes, which are used to compute the FFT of u, these coefficients are then multiplied by the imaginary unit (i) and the corresponding wavenumber (k_x,k_y), and the resulting Fourier coefficients are then transformed back to physical space through a inverse FFT. The values of the approximate derivative are thus given by

$$\frac{\partial \theta_N}{\partial x}(x,y,z) = \sum_{k_x}\sum_{k_y} ik_x(\hat{\theta}(k_x,k_y,z))\exp(i[k_x x + k_y y]), \tag{3.6}$$

$$\frac{\partial \theta_N}{\partial y}(x,y,z) = \sum_{k_x}\sum_{k_y} ik_y(\hat{\theta}(k_x,k_y,z))\exp(i[k_x x + k_y y]), \tag{3.7}$$

where $\frac{\partial \theta_N}{\partial x_i}$ is the Fourier series of the derivative of θ. Recall that to obtain a real valued approximate derivative of θ one needs to omit the Nyquist frequency wavenumber from the summations (Albertson and Parlange, 1999b). For a discussion on Spectral methods in single domains see (Canuto et al., 2006). Vertical derivatives are computed with second order accurate centered finite differences. The values of the approximate vertical derivatives at each layer in the computational grid $z(i)$ are given by:

$$\frac{\partial \theta_N}{\partial z}(x,y,z(i)) = \sum_{i=1}^{N_z} \frac{\theta_N(x,y,z(i+1)) - \theta_N(x,y,z(i))}{\Delta z}. \tag{3.8}$$

Note that with this approach derivatives of variables defined on the regular grid are stored in the staggered grid, and viceversa. For instance $\frac{\partial w}{\partial z}$ is stored in the staggered grid, whereas $\frac{\partial u}{\partial z}$ and $\frac{\partial v}{\partial z}$ are stored in the regular grid.

3.1.3 Aliasing errors

The principal algorithmic advantage of Pseudospectral collocation methods, when compared against pure spectral methods, for the solution of the Navier-Stokes equations

is the evaluation of the non-linear terms. Consider the truncated series expansion

$$\hat{s}_k = \sum_{m+n=k;|m|,|n|<N/2} \hat{\theta}_m \hat{\xi}_n, \qquad |k| \leq N/2 \tag{3.9}$$

where N denotes the number of collocation points in the considered interval, and k are the available wavenumbers $(-N/2 \leq k \leq N/2-1)$. The direct summation implied by Eq. 3.9 takes $O(N^2)$ operations. In three dimensions, the cost would be $O(N^4)$, provided that one utilizes the tensor-product nature of multidimensional spectral approximations (Orszag, 1980), which is prohibitively expensive, especially when one considers that for a nonlinear term a finite-difference algorithm takes $O(N)$ operations in one dimension (and $O(N^3)$)in three (Canuto et al., 2006). However, the use of transform methods enables evaluate Eq. 3.9 in $O(Nlog2N)$ operations (and the three-dimensional generalization in $O(N3\log 2N)$ operations). This technique was developed independently by Orszag (1969b, 1970) and Eliasen et al. (1970) and it enabled the use of spectral methods for large-scale computations. In Pseudospectral collocation algorithms non-linear terms are evaluated directly in physical space, leading to aliasing errors in the computation of $\hat{s}_k$. To illustrate the point, we introduce the discrete transforms

$$\theta_j = \sum_{k=-N/2}^{N/2-1} \hat{\theta}_k e^{ikx_j} \qquad j = 0,1,2\ldots N-1, \tag{3.10}$$

$$\xi_j = \sum_{k=-N/2}^{N/2-1} \hat{\xi}_k e^{ikx_j} \qquad j = 0,1,2\ldots N-1, \tag{3.11}$$

and define

$$s_j = \theta_j \xi_j \qquad j = 0,1,2\ldots N-1, \tag{3.12}$$

and

$$\tilde{s}_k = \frac{1}{N}\sum_{j=0}^{N-1} s_j e^{-ikx_j}, \qquad k = -\frac{N}{2},\ldots,\frac{N}{2}-1, \tag{3.13}$$

where

$$x_j = 2\pi j/N. \tag{3.14}$$

Note that the $\tilde{s}_k$ are the discrete Fourier coefficients of the function s. The use of discrete transform orthogonality relations results in

$$\tilde{s}_k = \sum_{m+n=k} \hat{\theta}_m \hat{\xi}_n + \sum_{m+n=k\pm N} \hat{\theta}_m \hat{\xi}_n = \hat{s}_k + \sum_{m+n=k\pm N} \hat{\theta}_m \hat{\xi}_n. \tag{3.15}$$

The second term on the right-hand side is the so-called aliasing error. Given that if the convolution sums are evaluated as described above, the differential equation is not approximated by a true spectral Galerkin method. The generalization of the pseudospectral evaluation of convolution sums to more than one dimension is straightforward. Several techniques have been developed to remove the aliasing error from Eq. 3.15; in this study we adopt the 3/2 rule, which is described in the following.

Removal of aliasing errors

Within the previously introduced one dimensional framework it is possible to eliminate the aliasing errors in the evaluation of non-linear terms using a discrete transform with $M = 3N/2$ rather than N points in their evaluation, as shown in the following. Assuming

$y_j = 2\pi j/M$ we define

$$\overline{\theta}_j = \sum_{k=-M/2}^{k=M/2-1} \breve{\theta}_k e^{iky_j}, \tag{3.16}$$

$$\overline{\xi}_j = \sum_{k=-M/2}^{k=M/2-1} \breve{\xi}_k e^{iky_j}, \tag{3.17}$$

$$\bar{s}_j = \theta_j \xi_j \tag{3.18}$$

for $j = 0,1,2,\ldots,M-1$, where $\breve{\theta}_k$ are the $\hat{\theta}_k$ coefficients in the range $|k| \lessapprox N/2$, and zero otherwise. They're the $\hat{\theta}_k$ padded with zeros for the additional wavenumbers. Let

$$\breve{s}_k = \frac{1}{M} \sum_{j=0}^{M-1} \bar{s}_j e^{-iky_j}, \qquad k = -\frac{M}{2}, \ldots, \frac{M}{2} - 1, \tag{3.19}$$

then we have

$$\breve{s}_k = \sum_{m+n=k} \breve{\theta}_m \breve{\xi}_n + \sum_{m+n=k\pm M} \breve{\theta}_m \breve{\xi}_n, \tag{3.20}$$

where the second term on the RHS of Eq. 3.20 is the aliasing error. Since we are interested in $\breve{s}_k$ for $|k| \leq N/2$, we choose M so that the second term on the right-hand side vanishes for these k, which holds for

$$M \geq \frac{3N}{2} - 1 \tag{3.21}$$

With $M = \frac{3N}{2}$ we thus obtain de-aliased coefficients, which allow for a proper evaluation of the nonlinear terms.

3.1.4 Time integration

The fractional step method (Chorin, 1968; Kim and Moin, 1985) is adopted to solve the system defined by Eq. 3.1. It consists of two (fractional) steps. At the first step an

intermediate velocity field is computed as follows:

$$\tilde{u}^{*}_{N,i} = \tilde{u}^{n}_{N,i} + \frac{3}{2}\Delta t RHS^{n}_{i} - \frac{1}{2}\Delta t \left[RHS^{n-1}_{i} - \frac{\partial \tilde{\pi}_N}{\partial x_i}^{n-1} + \tilde{f}^{n-1}_{N,i}\,\delta(x_i - x_i^{\Gamma_b}) \right] \tag{3.22}$$

where

$$RHS^{n}_{i} = u^{n}_{N,j}\left(\frac{\partial \tilde{u}_{N,j}}{\partial x_i} - \frac{\partial \tilde{u}_{N,i}}{\partial x_j}\right)^{n} + \left(\frac{\partial \tau^{SGS}_{N,ij}}{\partial x_j}\right)^{n} - \frac{1}{\rho}\frac{\partial \tilde{p}_{\infty}}{\partial x_i}\delta_{i1} \tag{3.23}$$

Then at the second step $\tilde{u}^{*}_{N,i}$ is corrected to give the new velocity $\tilde{u}^{n+1}_{N,i}$ as follows

$$\tilde{u}^{n+1}_{N,i} = \tilde{u}^{*}_{N,i} - \frac{3}{2}\Delta t \frac{\partial \tilde{\pi}_N}{\partial x_i}^{n} + \tilde{f}^{n}_{N,i}\delta(x_i - x_i^{\Gamma_b}), \tag{3.24}$$

where $\tilde{f}^{n}_{N,i}$ is computed to provide a zero velocity at the nodes inside the interface Γ_b:

$$\tilde{f}^{n}_{N,i} = 3/2\frac{\partial \pi^{n}_{N}}{\partial x_i} - u^{*}_{i}/\Delta t. \tag{3.25}$$

Computing the divergence of Eq. 3.24 and enforcing the incompressibility constraint $\frac{\partial \tilde{u}^{n+1}_{N,i}}{\partial x_i} = 0$, results into a Poisson equation for the modified kinematic pressure:

$$\frac{\partial^2 \tilde{\pi}^{n}_{N}}{\partial x_i^2} = \frac{2}{3\Delta t}\frac{\partial \tilde{u}^{*}_{N,i}}{\partial x_i} + \frac{\partial \tilde{f}^{n}_{N,i}}{\partial x_i}\delta(x_i - x_i^{\Gamma_b}). \tag{3.26}$$

Equations 3.25 and 3.26 are coupled and can be solved iteratively till the numerical solution for $\tilde{\pi}^{n}_{N}$ and $\tilde{f}^{n}_{N,i}$ converges. The Poisson Eq. 3.26 for pressure with the Neumann boundary condition on the top and bottom boundaries is solved by using the previously described pseudospectral transform in the horizontal and second-order centered finite differences in the vertical, resulting in a tridiagonal system, which is solved relying on the efficient Thomas algorithm.

3.1.5 Subgrid-scale model

In the proposed study we consider two LES closure models for the subgrid-scale terms τ_{ij}^{SGS}: the classic static Smagorinsky model (Smagorinsky, 1963) in conjunction with a wall damping function (SMAG), similar to that adopted in (Mason and Thomson, 1992), and the Scale dependent model with Lagrangian averaging of the coefficient (LASD) developed in Bou-Zeid et al. (2005).

Smagorinsky models rely on the viscous analogy and on the mixing length concept, and evaluate the subgrid-scale terms as a function of the resolved strain rate tensor:

$$\tau_{ij}^{SGS} = -2\nu_t \tilde{S}_{ij} = -2(c_{s,\Delta}\Delta)^2 \|\tilde{S}\|_2 \tilde{S}_{ij}, \tag{3.27}$$

where ν_t represents the eddy viscosity, Δ is the filter width (usually proportional to the grid size), $\tilde{S}_{ij}$ is the filtered shear rate tensor and $c_{s,\Delta}$ is the Smagorinsky coefficient at scale Δ. The two models essentially differ in the way they compute the Smagorinsky coefficient.

The SMAG model prescribes a constant coefficient, whose value is usually the one derived from the theory of homogeneous turbulence ($c_{s,\Delta} = 0.16$, for the sharp spectral cutoff filter). However, in applications involving high Reynolds number boundary layer flows – such as the one proposed herein – the model is known to be over-dissipative in the near wall regions, where $c_{s,\Delta}$ should approach zero. To cope with this we introduce an empirical wall damping function (Mason and Thomson, 1992), which has the drawback of requiring an ad-hoc calibration for each specific flow case, but partially ameliorate the dissipative properties of the SMAG model.

The LASD model overcomes the necessity of ad-hoc specification of the damping function by using the smallest resolved scales to compute the model coefficient at runtime. It represents an evolution of the original dynamic model, based on the Germano identity (Germano et al., 1990) and it's modifications (Lilly, 1992). LASD relaxes the scale invariance assumption of the model coefficient, which is a desirable

property in the near wall regions, where the grid size approaches the limits of the inertial subrange (Meneveau and Katz, 2000). The Lagrangian averaging of the model coefficient makes the model well suited for applications with heterogeneous spatial conditions since it preserves local variability, while satisfying Galileian invariance, and overcoming the requirement of homogeneous directions (Bou-Zeid et al., 2005). Further, along fluid pathlines the energy cascade process is more apparent (Meneveau and Lund, 1994), which enforces the theoretical basis of the model. To reduce the strong Gibbs oscillations that would arise at the interface if adopting a classic spectral cutoff filter, a Gaussian filter is introduced in conjunction with the LASD model, which has the desirable property of being of compact support in both physical and wavenumber space (Tseng et al., 2006).

3.1.6 Discrete forcing immersed boundary method (IBM)

To model the urban canopy a discrete forcing approach immersed boundary method is adopted (Mittal and Iaccarino, 2005; Mohd-Yusof, 1997). The buildings' interface $\Gamma_b(x,y)$ is represented implicitly as the zero level-set of a (higher dimensional) signed distance function $\phi(x,y,z)$, and the computational domain Ω is splitted in two regions, the inside building region Ω_k, where $\phi < 0$, and the atmosphere region Ω_a, where $\phi > 0$, as displayed in figure 3.1. A specific algorithm was implemented to build the $\phi(x,y,z)$ function, based on an iterative projection technique, which accepts triangulated surfaces as input. The immersed boundary algorithm is a minor modification of the one proposed in (Chester et al., 2007). The normal-to-wall velocity component $u_i^n = (u_j n_j) n_i$, where $n_i = \partial\phi/\partial x_i$, is fixed to zero at Γ_b through the forcing term defined in Eq. 3.25 (penalty method) and and a law of the wall is applied at all the collocation nodes which fall in the region $-1.1\Delta \leq \phi \leq 1.1\Delta$, where $\Delta = (dx \cdot dy \cdot dz)^{1/3}$. The law of the wall is based on the equilibrium logarithmic assumption (Monin and Obukhov, 1954). Given that our roughness elements are relatively bluff and sharp edged the skin friction component of the stress is negligible, when compared to the wall normal

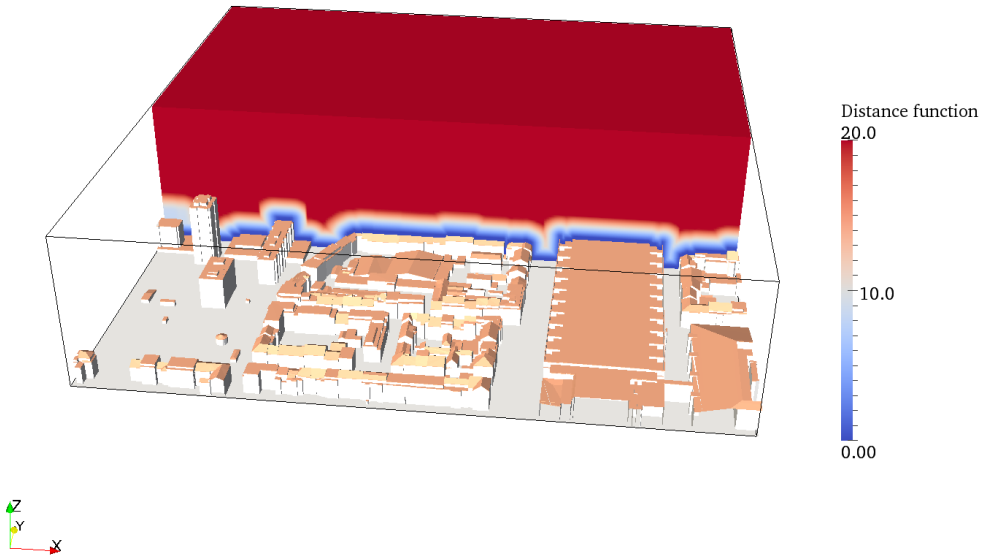

Figure 3.1: Color contour of the distance function $\phi[x,y,z]$ for a $512 \times 512m$ subset centered at the tower location. The three-dimensional domain (see black outline) has been clipped at the plane $y = 256m$ and the colormap has been clipped to $\max(\phi) = 20m$ for ease of visualization.

component; in flows where the skin friction is important, improvements can be made to accommodate more sophisticated wall models.

The main difficulty in coupling the immersed boundary method with a pseudospectral algorithm is represented by the fact that the domain is not simply connected. If $\phi \leq 0 \Rightarrow u_i = 0$, then we have that our solution, in a given plane cutting the building elements, is piecewise smooth ($C^?$), with the discontinuities localized at the building-atmosphere interface Γ_b. The spectral representation will result in Gibbs oscillations in the near interface regions, which will then propagate away from the

singularity, and, hence, degrade the quality of the partial sum approximation (Greer and Banerjee, 1997). To partially alleviate such phenomena a smooth velocity profile $\tilde{u}_i$ is generated in Ω_k ($\phi \leq 0$), before the spectral differentiation step, adopting a Laplacian smoothing operator iteratively (Tseng et al., 2006), with:

$$\tilde{u}_k^{new}(i,j) = (1-4\lambda)\tilde{u}_k^{old}(i,j) + \lambda(\tilde{u}_k^{old}(i+1,j) + \tilde{u}_k^{old}(i-1,j) + \tilde{u}_k^{old}(i,j+1) + \tilde{u}_k^{old}(i,j-1)) \tag{3.28}$$

where $\lambda = 0.24$. The approach resembles well known reconstruction schemes (Cai et al., 1989; Greer and Banerjee, 1997).

3.1.7 Site description and instrumentation

We use field data that were collected during the Basel Urban Boundary Layer Experiment (BUBBLE), a multi-institutional effort dedicated to the energetics and dispersion processes in the urban boundary layer (Rotach et al., 2005).

During BUBBLE, a 32 m high tower was deployed inside the 13 m wide Sperrstrasse street canyon in Basel, Switzerland $(47°33'57.20"\text{N}, 7°35'48.80"\text{E}, \text{WGS}-84)$. The orientation of the street canyon is along the axis $066° - 246°$ (ENE to WSW), the block where the tower was operated is characterized by a length of 160 m, and an average width-to-height ratio of $\xi_c/z_h = 1.0$, where ξ_c is the street canyon width and where z_h is the mean building height. The tower was placed at the midpoint of the block, 3 m away from the north wall, and equipped with six ultrasonic anemometer-thermometers (labels $A-F$ in table 3.1), which were mounted on horizontal booms reaching from the tower into the centre of the street canyon.

Buildings on both sides of the street canyon "Sperrstrasse" have pitched roofs except two flat-roof buildings directly adjacent to the tower on the northern side (label 1 and 2) and two flat-roof buildings close to the two intersections (label 3 and 4). The

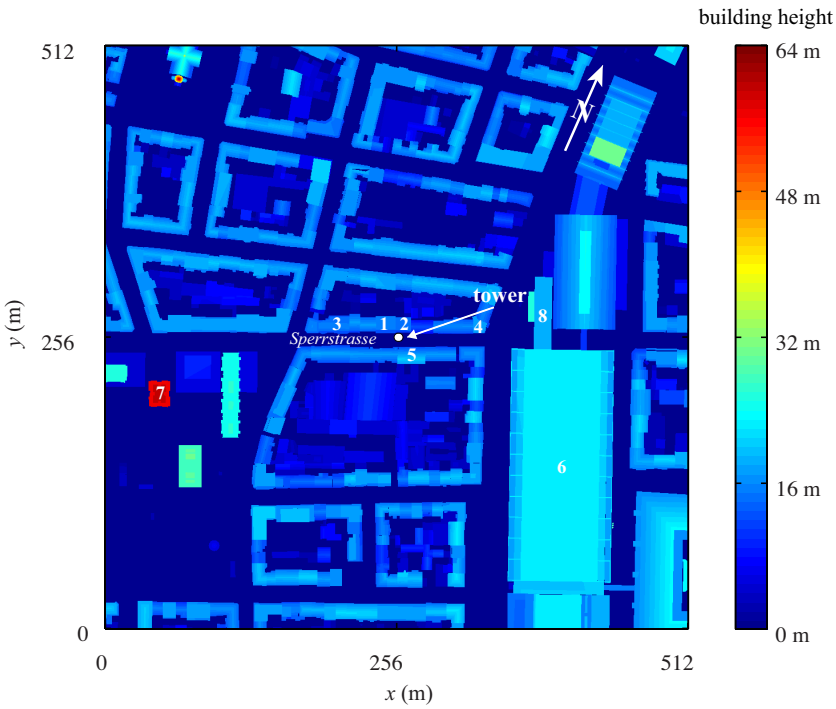

Figure 3.2: Color contour of the surface height $(\Gamma_b(x,y))$ for a neighborhood scale of 512×512 m, centered at the tower location. The Sperrstrasse street canyon is aligned with the x coordinate axis.

height of buildings typically reaches 15 m on both sides. A high pitched roof of 20 m is located directly to the south-east of the tower (label 5) (Christen et al., 2009). Sectors from west to NNE and SSE to SSW are similar to structures found immediately around the tower. These sectors are homogeneous in terms of integral morphometric statistics and building height with fetch extending to 700 m. In the sector NE to SSE an extensive commercial area is found at 100 m distance to the tower with flat roofs and roof heights from 20 m to 25 m (label 6), whereas an isolated high-rise building of 64 m height is located $\approx$ 200 m to the south-west of the tower (label 7). A 18.5 m building is located approximately 100 m north-east of the tower (label 8).

Table 3.1: Details on the ultrasonic anemometer-thermometer (sonic) instrumentation, label, absolute measurement heights z, normalized measurement heights (the normalization scale is the location of the highest anemomether-thermometer) z/z_h, sonic type, sampling frequency f (Hz).

Label	z (m)	z/z_t	Instrument type	f (Hz)
A	3.6	0.11	Gill R2 Omnidirectional	20.8
B	11.3	0.35	Gill R2 Omnidirectional	20.8
C	14.7	0.46	Gill R2 Omnidirectional	20.8
D	17.9	0.56	Gill R2 Omnidirectional	20.8
E	22.4	0.7	Gill R2 Asymmetric	20.8
F	31.7	1	Gill HS	20.0

* The labels are matching those in figure 3.3.

3.1.8 Processing of the profile tower dataset

Wind components u, v, w and virtual acoustic temperature θ were continuously recorded at all six levels simultaneously from December 1, 2001 to July 15, 2002. Data acquisition systems and quality control procedures including wind-tunnel calibrations of the instruments are described and documented in Christen (2005a). u, v and w statistical moments up to order three were calculated and stored for blocks over 5 minutes. No filtering was applied to the signal nor standard de-trending, to ensure energy conservation and enable vertical gradients of the state variables to be properly computed. To provide data for comparison with pressure driven simulations the following processing is further performed:

1. data are averaged in blocks of 30 minutes;

2. data are selectively sampled from the year-round dataset based on the wind direction computed at the tower top sensor. Only $30'$ blocks characterized by

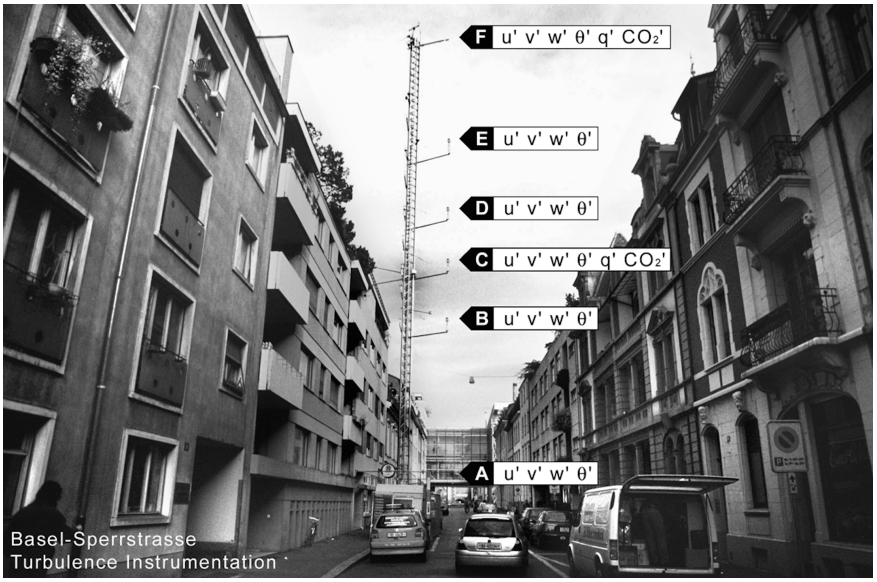

Figure 3.3: Photo of the profile tower, taken from inside the street canyon with view towards EEN. Photo credit: Prof. A. Christen.

an approaching wind direction of $\alpha = 66^\circ \pm 10^\circ$ (along canyon regimes) and of $\alpha = 156^\circ \pm 10^\circ$ (across canyon regimes) throughout the 6×5 min intervals are kept;

3. in order to eliminate the influence of thermal stability, the periods are further filtered based on the classic stability parameter $\zeta = (z-d)/L$ (Stull, 1988), where L is the Obukhov length ($L = \theta u_\tau^2/[\kappa g \theta_*]$) calculated with both scaling velocity u_τ and scaling temperature θ_* measured at the tower top. Only periods characterized by near-neutral stability are kept, $-0.1 \leq \zeta \leq +0.1$. The displacement height is computed as $d = 2/3 z_h$, in the typical range suggested for high-density urban roughness elements with skimming flow (Grimmond and Oke, 1999);

4. cases characterized by $u_\tau \leq 0.15$ ms^{-1} at tower top are excluded from the

analysis.

The availability of a relatively long dataset allowed to obtain blocks satisfying the above (strict) requirements. In the specific, we obtained 30 blocks for the ENE wind direction ($\alpha = 66^{\circ\pm10^{\circ}}$) and only 3 blocks for the SSE direction ($\alpha = 156^{\circ\pm10^{\circ}}$).

3.1.9 Averaging procedures

Throughout the study we will adopt the double averaged DA approach to describe the flow field. The DA methodology has been initially developed to study flow over vegetation canopies (Finnigan et al., 1984; Raupach and Shaw, 1982; Wilson and Shaw, 1977) and extended in studies of flow over gravel beds (Nikora et al., 2001, 2007) and over rigid canopies (Coceal et al., 2006; Raupach et al., 1991). In the DA framework a general variable $\theta(x,y,z)$ is decomposed into a time-space average $\langle\overline{\theta}\rangle(z)$ (bar and brackets denote temporal and spatial averages, respectively), into a fluctuation of the time averaged quantity with respect to its time-space value $\overline{\theta}''(x,y,z)$ and in a turbulent fluctuation θ':

$$\theta(x,y,z,t) = \langle\overline{\theta}\rangle(z) + \overline{\theta}''(x,y,z) + \theta'(x,y,z,t). \tag{3.29}$$

We here consider the intrinsic averaging approach (Nikora et al., 2007), where averaging is performed over horizontal planes in the fluid domain only, i.e. only the outdoor air, excluding the air volume within buildings, as opposite to the superficial spatial averaging $\langle\overline{(\cdot)}\rangle_s$ where averaging is performed over the whole horizontal plane (x,y), including the interior of the roughness elements.

CHAPTER 4

Sensitivity analysis: domain size requirements

4.1 Introduction

Over realistic urban surfaces, the atmospheric flow is spatially variable and characterized by a broad range of scales (Barlow, 2014; Barlow and Coceal, 2009; Belcher, 2005; Raupach et al., 1991; Roth, 2000). When performing LES simulations over realistic urban canopies it is necessary to isolate a representative subset of the considered surface, which allows to obtain representative DA profiles and to fully represent the main dynamical modes in the boundary layer, while minimizing computational costs. Further, a careful choice of the computational domain is of fundamental importance for the sake of comparison between LES results and full scale measurements, given that the influence of a single building on the flow downwind can be several times its characteristic size. This chapter aims at determining (1) the optimal domain size that allows for a proper comparison with point-wise tower measurements,

and (2) what is the extend of a representative subset, centered at the tower location, for the current surface. To do so, we perform a series of runs varying the horizontal and vertical extent of the regular domain Ω, considering two angles of approaching wind direction, one in the along (WSW) and one in the cross canyon direction (NNW). Other numerical parameters such as grid stencil, imposed pressure gradient, time-step and number of integration steps are kept constant across the runs, to allow for an objective comparison (see Table 5.1).

The effect of varying domain size on DA and local (tower location) mean flow and turbulent production rates is analyzed. Throughout the study, we will assume the boundary layer is fully developed and drive the flow in simulations adopting a constant pressure gradient $\frac{1}{\rho}\frac{\partial \tilde{p}_\infty}{\partial x}$, which represents an alternative to the common approach of imposing a turbulent inlet boundary conditions. This forcing is justified given the relatively homogeneous integral morphometric statistics and building height in the neighborhood. In order to reduce the computational costs we rely on the common approach of sacrificing the $\delta/z_h \gtrapprox 50$ requirement, our δ/z_h varies in the range $[8.4, 25.7]$ (see Table 5.1). All simulations are run at a vertical and horizontal resolution of $z_h/\Delta_z \approx 8$. Roughness has a great influence on turbulence up to $z/z_h = \min(1 + D/z_h, 5)$ (Jimenez, 2004; Raupach and Thom, 1981), where D is the minimum interspacing assuming $z/z_h = 5$, based on the morphometric characteristics of the subset, and given that the extent of the logarithmic layer is $\approx 0.15\delta$, we cannot expect the ISL to survive. The limited δ/z_h in the proposed study might be justified by considering that the focus is on the surface layer up to $z = z_t$, where $z_t = 32$ m is the location of the highest anemometer in the profile tower; in these regions turbulence is expected to be strongly affected by the surface details and only in minor part by dynamics of the outer layer (as will be shown in the following sections). As the horizontal extent of the computational domain is reduced across the runs the integral morphometric statistics of the surface also change (see Table 4.2), therefore resulting in a modification of the integrated hydrodynamic roughness length z_0 and of the

displacement height d which, together with the friction velocity u_τ, are the common scaling parameters in the surface layer. Given the difficulties connected with a strict definition of z_0 and d under the given setting, we drop the standard surface layer scaling, and instead use the tower height z_t and the time averaged stream-wise velocity at the tower top $u(z_t)$ as characteristic length and velocity scales.

4.2 Setup of the simulations

As stated in the introduction, we perform a series of runs varying both the horizontal and the vertical domain size, and considering two angles of approaching wind direction (WSW and NNW). Grid stencil and numerical parameters are kept constant across simulations, to allow for an objective comparison (see Table 5.1).

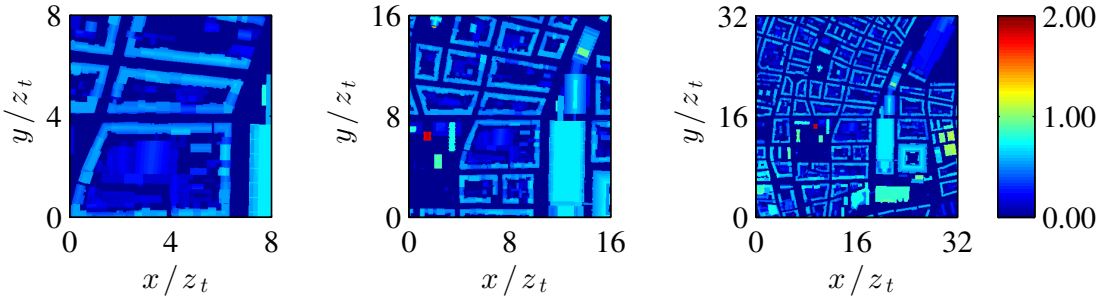

Figure 4.1: Normalized surfaces' height (z/z_t) centered at the tower location.

The digital surface models $\Gamma_b(x,y)$ are displayed in Figure 4.1, geometrical and statistical properties of the surface are highlighted in Table 4.2 whereas parameters for each run are summarized in Table 5.1.

The flow is forced by imposing a constant pressure gradient $\partial_x p_\infty = 0.004$ Nm^{-3}, which defines a friction velocity $u_\tau^2 = (\delta - d)\partial p_{x,\infty}/\rho \approx 1$ m s^{-1}, making the system independent from the Reynolds number (fully rough flow regime). Under such conditions it is possible to scale the solution throughout the boundary layer with a

Table 4.1: Geometrical and numerical parameters for the LES runs.

Label	L_x, L_y, L_z (m)	$nx \times ny \times nz$	δ/z_h	$\measuredangle$ (°)
A	$1024^2 \times 384$	$512^2 \times 192$	25.7	156
B	$1024^2 \times 256$	$512^2 \times 128$	17.2	156
C	$1024^2 \times 192$	$512^2 \times 96$	12.8	156
D	$512^2 \times 192$	$256^2 \times 96$	12.5	156
E	$512^2 \times 128$	$256^2 \times 64$	8.4	156
F	$256^2 \times 128$	$128^2 \times 64$	10.0	156
G	$1024^2 \times 384$	$512^2 \times 192$	25.7	66
H	$1024^2 \times 256$	$512^2 \times 128$	17.2	66
I	$1024^2 \times 192$	$512^2 \times 96$	12.8	66
L	$512^2 \times 192$	$256^2 \times 96$	12.5	66
M	$512^2 \times 128$	$256^2 \times 64$	8.4	66
N	$256^2 \times 128$	$128^2 \times 64$	10.0	66

* The computational domains are centered at the tower locations (x_t, y_t).

characteristic velocity U, being the molecular diffusion term in the LES equations negligible.

The modeled subgrid scale stresses are imposed through the standard equilibrium law of the wall (Monin and Obukhov, 1954) fixing $z_0 = \Delta/15$. z_0 is chosen based on the Nyquist-Shannon representation criteria (Shannon, 1993): adopting a grid stencil Δ the smallest flow/surface feature we can directly represent through our Fourier partial sums is $k_\Delta = 2\Delta$ meaning that all scales smaller than k_Δ will need to be modeled. Given that $z_0 = 0.033 k_s$ and since $k_s \to k$ in the limit of negligible viscous effects, we have that $z_0 = 0.033 k_\Delta \approx \Delta/15$. However, the influence of the model parameter z_0 on the solution is negligible, being most of the surface drag generated by resolved (in the LES

Table 4.2: Morphometrical statistics/parameters derived from the raster based surface models for the different surfaces. z_h represents the average roof's height, σ_{z_h} is the standard deviation of the roofs heights, $\overline{\Gamma}_\mathrm{b}$ is the average surface height, $\sigma_{\Gamma_\mathrm{b}}$ is the standard deviation of the surface heights and λ_p is the building area fraction at the first layer of collocation nodes in the staggered grid ($z = \Delta_z/2$).

L_x, L_y m	z_h (m)	σ_{z_h} (m)	$\overline{\Gamma}_\mathrm{b}$ (m)	$\sigma_{\Gamma_\mathrm{b}}$ (m)	$\lambda_p(z = \Delta_z/2)$
1024^2	14.9	6.8	6.9	8.8	0.46
512^2	15.3	6.5	7.6	8.9	0.49
256^2	12.8	5.9	6.8	7.7	0.53

* The surfaces are centered at the tower location (x_t, y_t).

sense) pressure forces

$$F_i(z) = \int_S \tilde{p}(z)\, \tilde{n}_i\, dS + \rho \int_S \tau_{ij}(z)^{\Delta,sgs}\, \tilde{n}_j\, dS \approx \int_S \tilde{p}(z)\, \tilde{n}_i\, dS, \tag{4.1}$$

where $\tilde{n}_j$ is the unit normal vector to the surface Γ_b and $F_i(z)$ is the DA total drag force at a given height z.

Equations are integrated in time for 500 non-dimensional time units z_h/u_τ (corresponding to 400'000 time steps with $\Delta_t = 0.02$ s ≈ 2 hours), where $u_\tau \approx \frac{1}{\rho}\frac{\partial \tilde{p}_\infty}{\partial x}(\delta - d) = 1$. 300 time units are required in order to achieve statistical stationarity in the velocity field ($\sigma[\int_\Omega 0.5u^2 dV] \approx \frac{1}{10}\int_\Omega 0.5u^2 dV$) and 200 time units are used for the averaging period, to ensure convergence of the computed statistics.

4.3 Analysis of the mean flow

We take simulations *A* and *G* as references in the current comparison given their relatively larger domain extent (see Table 5.1). Figures 4.2 and 4.3 show the spatial variability of the time-averaged velocity field $\overline{u}$ along selected planes from simulation *G*.

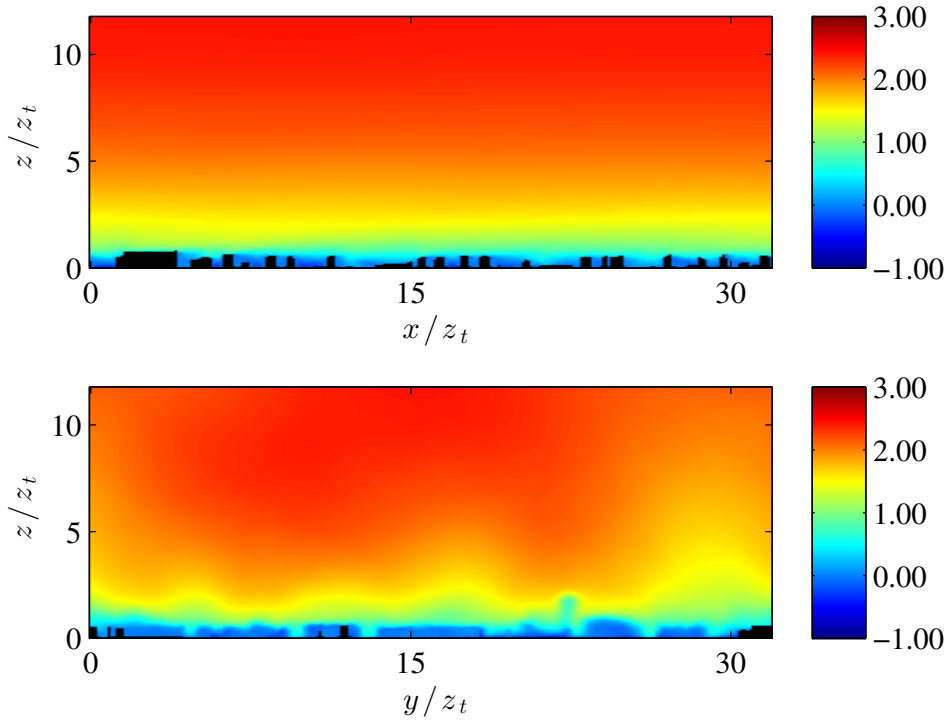

Figure 4.2: Color contours of time averaged $(200T)$ stream-wise velocity, on the central planes $y = 16$ (above) and $x = 16$ (below) from simulation $G(32^2 \times 12)$. Wind approaches from NNW (across the Sperrstrasse canyon).

From 4.2 and 4.3 it's clear how the heterogeneity of the urban surface causes spatial variability in the time averaged stream-wise velocity field, spatial variability which extends up to the RSL (see Figure 4.3), where the time-averaged flow shows strong

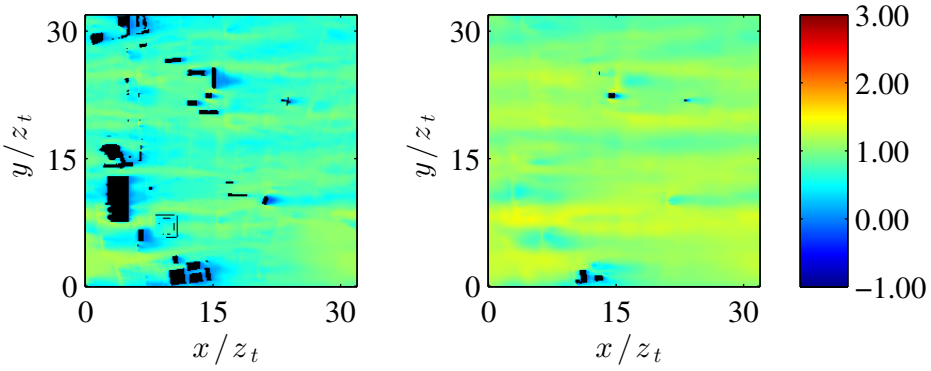

Figure 4.3: Color contours of time averaged $(200T)$ stream-wise velocity, on the plane $z/z_t = 0.8$ (left) and $z/z_t = 1$ (right) from simulation $G(32^2 \times 12)$. Wind approaches from NNW (across the Sperrstrasse canyon).

coherence in the stream-wise direction x. Figure 4.4 shows the normalized averaged one-dimensional velocity profiles at the tower location (x_t, y_t) for both the along and across-canyon wind approaching direction. To increase the number of samples and obtain good convergence of the estimators to the expected value, a spatial averaging has been performed on top of the time averaging, with compact support whose footprint is 6×6 m. A good collapse is observed at the heights of interest $(z/z_t \leq 1)$. The departure from the reference results (simulation A, G) at the height of the sonic anemometers is within 10% magnitude among all runs, underlying how the flow at these heights in the RSL is strongly dependent on local surface properties, and affected in minor part by outer layer dynamics. Profiles show exceptional collapse in the across-canyon flow direction (right plot in Fig. 4.4). In such settings a local updraft characterized the velocity field at the tower location (see Fig. 5.5), characterized by a zero $\overline{u}(x_t, y_t)$ velocity. Simulation F exhibits the largest departure from the reference profile for the along-canyon flow regime, mostly due to the relatively modest domain size.

Further, we are interested in defining how the spatial variability of the flow is modified from run to run, which will allow to have a better picture of the system,

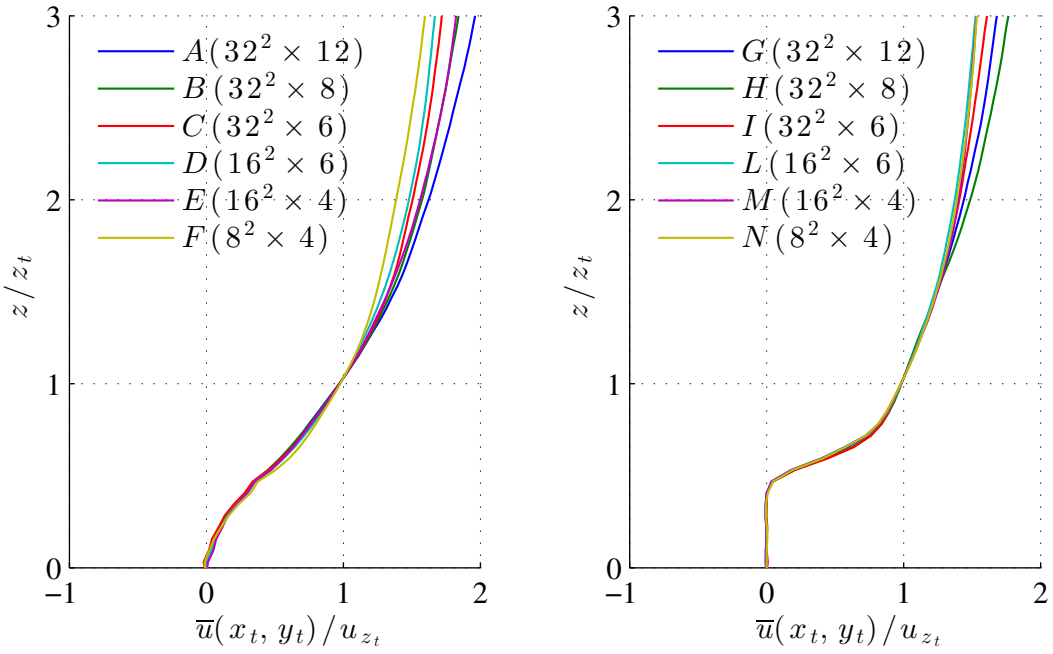

Figure 4.4: Comparison of time averaged $(200T)$ stream-wise velocity at the tower location (x_t, y_t) in the along canyon flow regime (left) and across canyon flow regime (right).

compared to simple one-dimensional plots. To do so, we compute the departure of time averaged velocity from its DA value as $\overline{\tilde{u}}''(z) = \overline{\tilde{u}}(z) - \langle\overline{\tilde{u}}\rangle(z)$ for each simulation i ($i = A,B,C,D,E,F,G,H,I,L,M,N$), and introduce the following scalar quantity

$$e_i = \overline{\tilde{u}}''_R - \overline{\tilde{u}}''_i\,, \tag{4.2}$$

where e_i defines the difference between the planar departures of the reference simulation (simulation A for the along-canyon regime and simulation G for the across-canyon regime), and the planar departures of the considered simulation i. e_i can be seen as a measure of the error in the spatial value of the mean velocity: if no differences

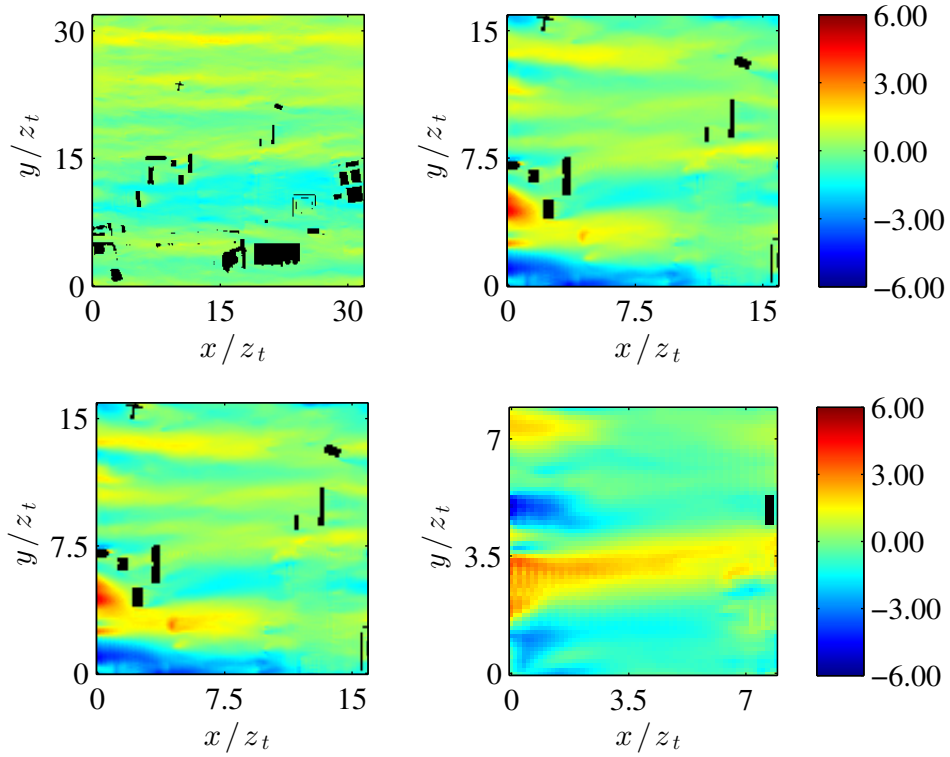

Figure 4.5: Color contours of e_i, $i =$ C, D, E, F, on the plane $z/z_t = 0.8$. From top-left to bottom-right results correspond to simulation $C(32^2 \times 12)$, $D(16^2 \times 6)$, $E(16^2 \times 4)$, $F(8^2 \times 4)$. Wind approaches from WSW (along the Sperrstrasse canyon).

between a given run (i) and the reference run (A or G, depending on the flow direction) holds, then $e_i = 0$ throughout the domain. Whenever a specific run exhibits stronger horizontal gradients in the time-averaged stream-wise velocity$(\partial_x\overline{\tilde{u}}, \partial_y\overline{\tilde{u}})$ compared to those in the reference simulation, this will result in $e_i \neq 0$ and its norm will define the magnitude of variation. We focus at the $z/z_t = 0.8$ plane (height of the sonic E in the tower). From Figures 4.5 and 4.6 we observe how a decrease in the vertical domain size, from $L_z/z_t = 12$ to $L_z/z_t = 6$ already affects the time-averaged velocity field, for both wind approaching directions, i.e. $e_C \neq 0$ and $e_I \neq 0$ in the plane $z/z_t = 0.8$. For instance,

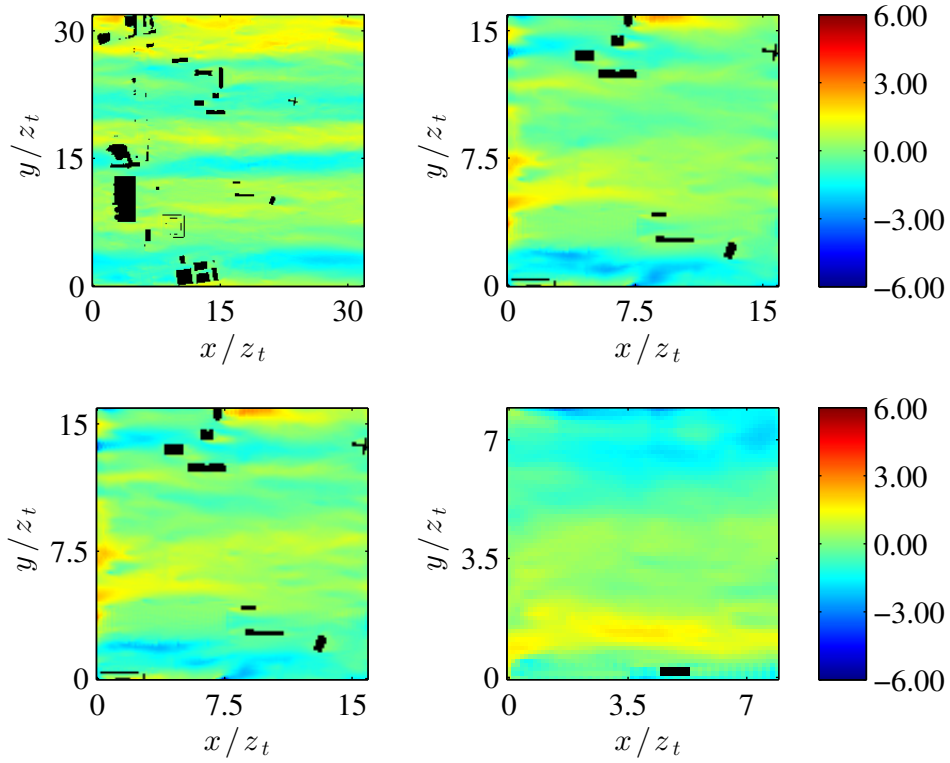

Figure 4.6: Color contours of e_i, $i = I, L, M, N$, on the plane $z/z_t = 0.8$. From top-left to bottom-right results correspond to simulation $I(32^2 \times 6)$, $L(16^2 \times 6)$, $M(16^2 \times 4)$, $N(8^2 \times 4)$. Wind approaches from NNW (across the Sperrstrasse canyon).

wake regions tend to be characterized by relatively higher velocities on average, due to the increased blockage. A decrease in the domain size has a stronger effect when the wind is in the along-canyon direction ($\alpha = 66^\circ$). In this regime departures are more apparent than for the $\alpha = 156^\circ$ wind direction (see Figure 4.5), in particular in the near boundary regions, where the enforced periodicity strongly modifies the mean flow patterns. $e_F \neq 0$ throughout the computational domain and its relatively high range of values reflects the presence of strong departures in the spatial distribution of the velocity field, with respect to the reference values. In the F run tower regions are

characterized by a relatively faster flow, connected with a high speed streak that is locked in place, most probably caused by the modest size of the computational domain, therefore severely modifying the picture throughout the computational domain. Since $e_D \approx e_E$, we identify simulation E as a possible candidate for the further comparison with tower measurements.

To shed additional light on the dynamics of turbulence, and to provide a more synoptic view of the system, in the following section we propose an analysis of the turbulent shear production rate.

4.4 Analysis of the turbulent shear production rate

A proper indicator of large scale active dynamics is the so-called shear production rate (P_s) of turbulent kinetic energy (TKE). When there is turbulent momentum flux in presence of mean shear the combination of the two tends to increase the turbulence levels (Stull, 1988), mostly at the large, anisotropic scales. This process is strongly linked to the vortex stretching mechanism, in which the energy injected into the system at a low wavenumber cascades to higher wave numbers (Pope, 2000). This process is particularly effective in eddies whose axis is aligned with the mean shear. The turbulent shear production rate is defined as follows:

$$P_s = -\overline{\tilde{u}_i' \tilde{u}_j'} \frac{\partial \overline{\tilde{u}}_i}{\partial x_j}, \tag{4.3}$$

where $i = 1,2,3$ are the three coordinate directions and $\overline{\tilde{u}_i' \tilde{u}_j'}$ is a velocity covariance. Figures 4.7 and 4.8 show the spatial variability of the time-averaged shear production rate P_s along the perpendicular planes that were selected for the velocity color contours (simulation G). Most of the TKE production occurs in the turbulent shear layers that separate from the roof top of the buildings, as apparent in Fig. 4.7, which are strongly dependent on the local structure of the surface, and can extend downstream up to several

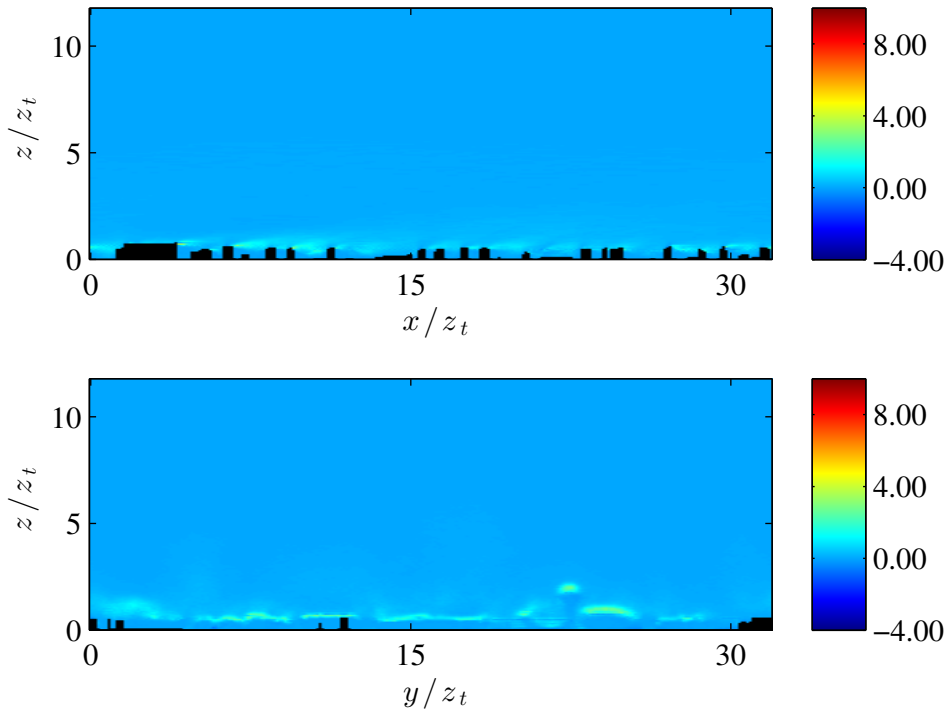

Figure 4.7: Color contours of the time averaged $(200T)$ shear production rate $P_s = \overline{\tilde{u}_i'\tilde{u}_j'}(\partial\overline{\tilde{u}}_i/\partial x_j)$ on the central planes $y = 16$ (above) and $x = 16$ (below) from simulation $G(32^2 \times 12)$. Wind approaches from north-west-north (across the Sperrstrasse canyon).

times the width of the building. The main components of P_s in these regions of the flow are $-\overline{\tilde{u}'\tilde{w}'}(\partial\overline{\tilde{u}}/\partial z)$ and $-\overline{\tilde{v}'\tilde{w}'}(\partial\overline{\tilde{v}}/\partial z)$, contributing up to 85% of the total production rate.

The time-average shear production rate, averaged over a 6×6 m horizontal area centered around the tower location (x_t, y_t), is shown in Figure 4.9 for both wind direction. Profiles have been normalized with the peak value $\max(P_s(z))$. A peak in the local production rate is apparent above z_h, for both the along and across canyon wind direction, mainly due the presence of thin shear layers in these regions of the

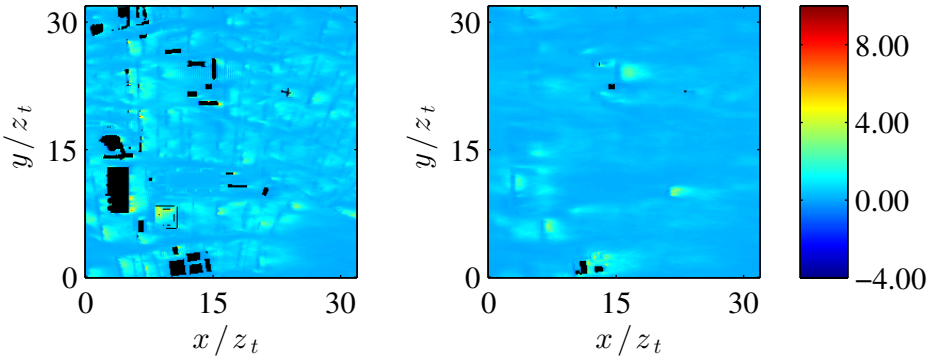

Figure 4.8: Color contours of the time averaged $(200T)$ shear production rate $P_s = \overline{\tilde{u}_i'\tilde{u}_j'}(\partial\overline{\tilde{u}}_i/\partial x_j)$, on the plane $z/z_t = 0.8$ (left) and $z/z_t = 1$ (right) from simulation $G(32^2 \times 12)$. Wind approaches from north-west-north (across the Sperrstrasse canyon).

flow (Cheng and Porté-Agel, 2013). The peak is particularly sharp in the across canyon direction. Departures in the production rates from the reference run (A) are within 5% in the regions of interest $(z/z_t \leq 1)$ for the across flow regime, underlying once again the poor influence of the domain size on the computed statistics.

The along flow regime in the left plot of Figure 4.9 shows instead how the production rates strongly depend on the actual domain size, and strongly departure from the reference value at the tower location in simulation F underlying the presence of a different equilibrium regime and somehow reflecting what Figure 4.5 had qualitatively suggested. Profiles from simulations B,C,D,E show a variation within 15% from the reference in $0 \leq z/z_t \leq 1$, therefore confirming once again simulation E and M (along and across-canyon wind approaching direction, respectively) as valid candidates for the further comparisons with experimental data.

In the upper part of the *RSL* and in the outer layer region $(z/z_t \gtrapprox 3)$ it is clear how increasing the domain size, in particular the height of the computational domain (δ) results in higher rates of production. For instance, from the right plot in Figure 4.9 (across-canyon regime) we observe very good matching between production rates of

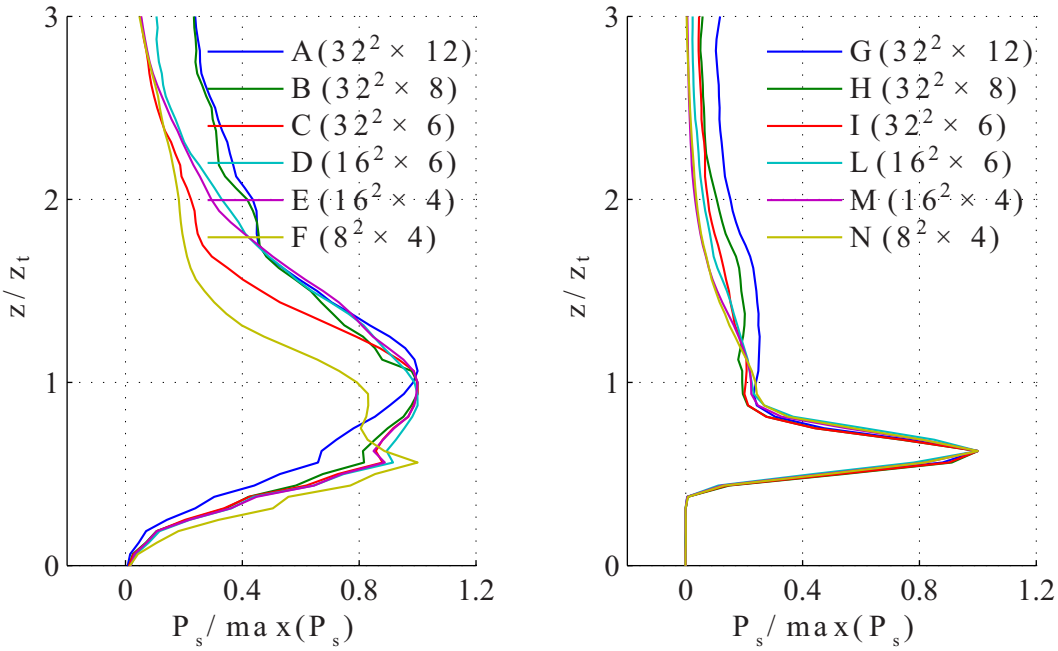

Figure 4.9: Comparison of time-averaged $(200T)$ normalized shear production rate at the tower location (x_t, y_t), for along-canyon (left plot) and across-canyon (right plot) wind approaching directions.

simulations $M-N$ and $I-L$, which are characterized by the same domain height δ. This increase in turbulent production in the outer layer is mainly a result of the imposed boundary conditions and constant pressure gradient driving the flow, which result in a linear variation with height of the total momentum flux in the vertical direction, as shown in the following.

4.5 Global statistics and representative subset

Given the essentially heterogeneous nature of the urban surface, morphometric statistics vary across the selected subsets (see Table 4.2). We here identify a

representative subset for use in the subsequent analyses. In order to do so, we focus on variations in DA quantities as a function of the horizontal and vertical extent of the computational domain. As shown in Figure 4.10, DA velocity profiles for simulations *F*

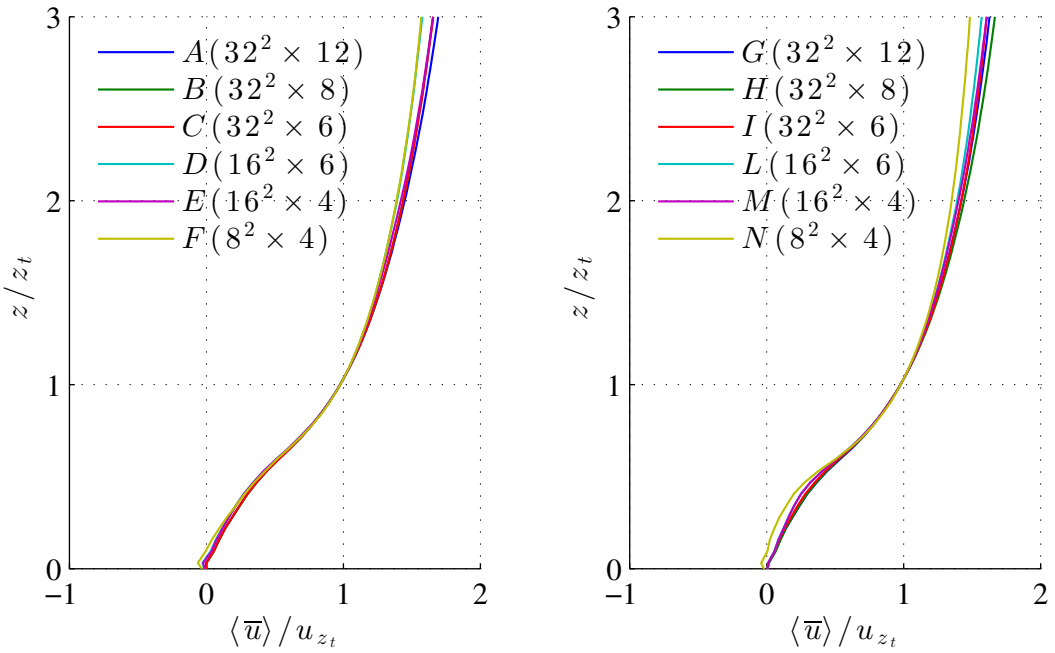

Figure 4.10: Comparison of DA stream-wise velocity profiles for along-canyon (left plot) and across-canyon (right plot) wind approaching direction.

and *N* (the smallest among the considered domains) depart significantly from the others DA velocity profiles in the regions of interest ($0 \leq z/z_t \leq 1$). As expected, domain height has essentially no influence on the DA averaged velocity profiles in the lower RSL, difference being $\lessapprox 10\%$ in magnitude at the heights of the sonic anemometers. Further up in the boundary layer departures are significant, but might reflect the limits of the proposed normalization, if adopted to compare profiles in the outer layer regions (the standard boundary layer scaling $[u_*, \delta]$ might be more appropriate in this case). Figure 4.11 displays a comparison of DA TKE shear production rates across the

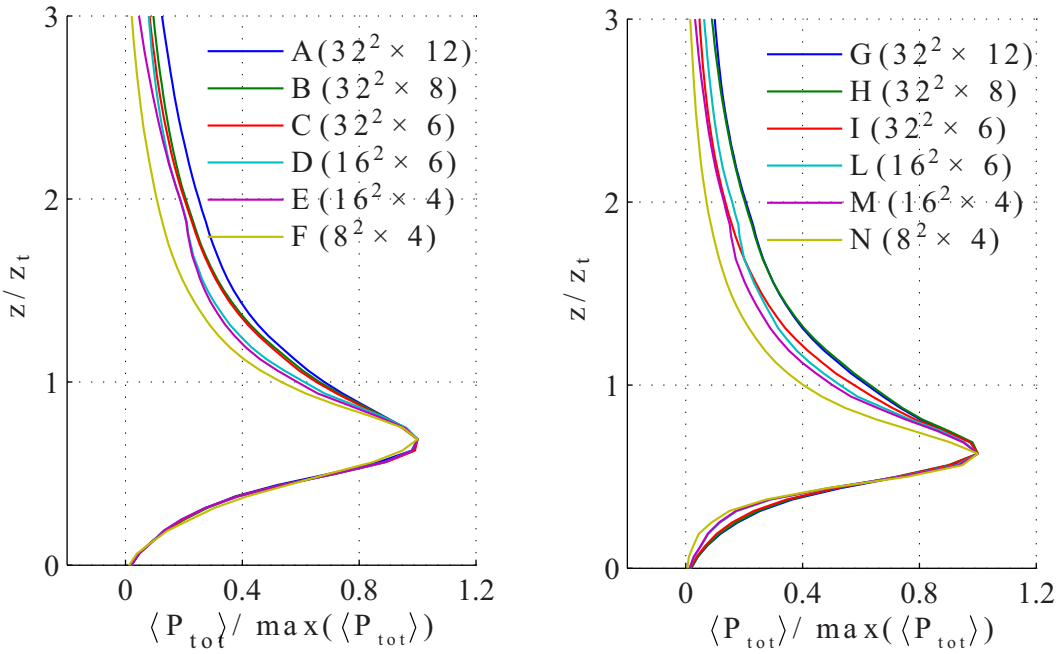

Figure 4.11: Comparison of DA total shear production rate $\langle P_{tot} \rangle$ for along-canyon (left plot) and across-canyon (right plot) wind approaching directions.

simulations for both winds regimes, where

$$\langle P_{tot} \rangle = \langle P_s \rangle + \langle P_w \rangle + \langle P_m \rangle = -\langle \overline{\tilde{u}_i' \tilde{u}_j'} \rangle \frac{\partial \langle \overline{\tilde{u}}_i \rangle}{\partial z} - \left\langle \overline{\tilde{u}_i' \tilde{u}_j'}'' \frac{\partial \overline{\tilde{u}}_i}{\partial z} \right\rangle - \langle \overline{\tilde{u}_i' \tilde{w}'} \rangle \left\langle \frac{\partial \overline{\tilde{u}}_i''}{\partial x_j} \right\rangle, \quad (4.4)$$

where the three terms on the RHS arise from the DA operation and are: shear production $P_s = -\overline{\tilde{u}_i' \tilde{w}'} \frac{\partial \overline{\tilde{u}}_i}{\partial z}$, wake production $P_w = -\left\langle \overline{\tilde{u}_i' \tilde{u}_j'}'' \frac{\partial \overline{\tilde{u}}_i''}{\partial x_j} \right\rangle$, work of the time-averaged velocity spatial fluctuations against the DA shear stress $P_m = -\langle \overline{\tilde{u}_i' \tilde{w}'} \rangle \left\langle \frac{\partial \overline{\tilde{u}}_i''}{\partial x_j} \right\rangle$. Profiles have been normalized with the peak total production value $\max(\langle P_{tot}(z) \rangle)$. The good matching across simulations in the regions of interest $0 \leq z/z_t \leq 1$ is apparent for the along canyon regime, whereas rather significant variations occur in the across

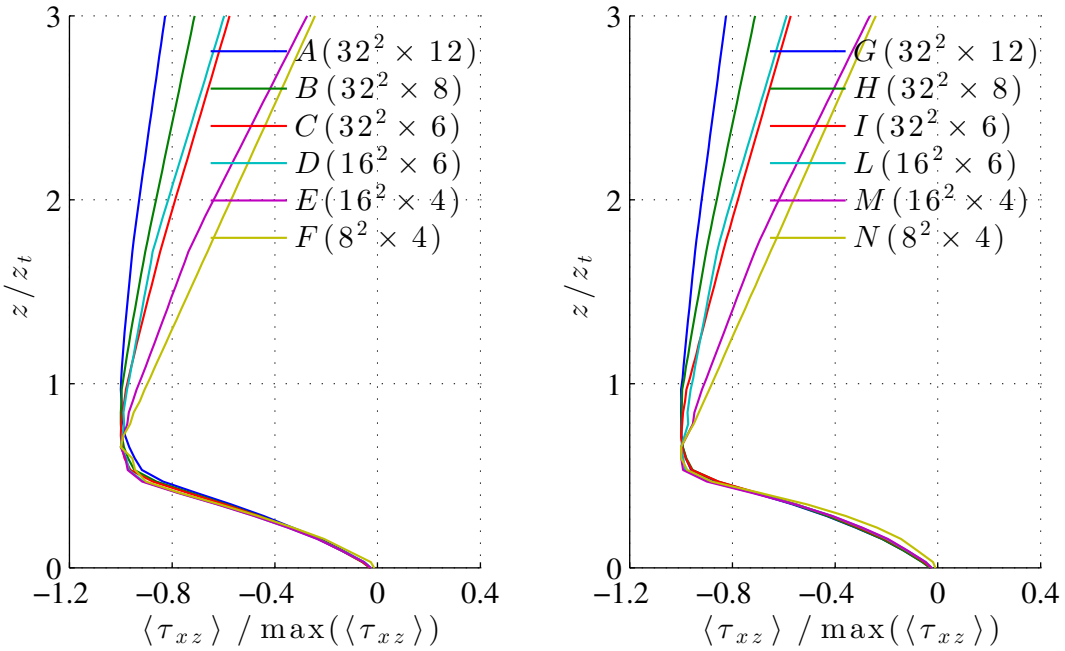

Figure 4.12: Comparison of DA total momentum flux (resolved + dispersive + subgrid) for along canyon (left plot) and across canyon (right plot) regimes. The form drag arising from the roughness elements is neglected.

flow regime. The horizontal domain size has strong effects on $\langle P_{tot}\rangle$ in the lower UCL ($z/z_t \lessapprox 0.5$), which vary $\propto L_x, L_y$. Immediately above the UCL ($0.5 \leq z/z_t \leq 0.8$) profiles in both flow regimes show good matching. In the core of the RSL $\langle P_{tot}\rangle$ shows strong variation for both wind regimes, this time being $\langle P_{tot}\rangle \propto L_z$. This mismatch is mainly due to the pressure gradient forcing approach, which forces the total vertical momentum flux to vary linearly in the upper regions of the boundary layer. This behavior is in contrast with the constant τ_{xz} value that characterizes zero-pressure-gradient atmospheric boundary layer flows in the ISL (Monin and Obukhov, 1954; Pahlow et al., 2001)). The linear variation with height of $\langle\tau_{xz}\rangle^{tot}(z)$ in the upper parts of the boundary layer is apparent from Fig. 4.12 for both wind regimes. This identity

for $\langle \tau_{xz} \rangle^{tot}(z)$ is therefore responsible for the observed mismatch in the $\langle P_{tot} \rangle$ profiles, since lower L_z forces $\langle \tau_{xz} \rangle^{tot}(z)$ to go to zero more rapidly.

Given the overall qualitative agreement between mean profiles and total production rates we identify the horizontal extend of the domain of simulations E and M as optimal for tower comparison and for the global analysis that will be proposed in the following sections.

CHAPTER 5

Spatial characterization of turbulence in the RSL and comparison with tower measurements

5.1 Introduction

As stated in Chapted 1, exchange processes between the UCL and the overlying atmosphere - including momentum transfer - are therefore simplified in a one-dimensional bulk flow representation, where the flow field is conceptually averaged in time and over a spatial subset of the urban canopy.

Proper techniques to reinstall a 1D approach in a truly three-dimensional RSL should account for the inherently variable canopy morphology, and its hierarchical structure of scales (from the street or canyon scale to the regional scale) as discussed in Britter and Hanna (2003).

In the current Chapter we use LES results to (1) characterize mean flow and turbulence in the RSL, (2) to determine the role of non-measurable terms such

as dispersive momentum fluxes, wake production, dispersive transport, pressure transport, dissipation of TKE, and (3) to determine how representative are single-point measurements, when used as surrogate for horizontally-averaged quantities over the entire urban domain. Such informations can then be used in order to guide and validate current upscaling for one-dimensional UCPs.

Justified by the results of the sensitivity analysis proposed in Chapter 4, we adopt the horizontal domain size of simulations *E* and *M* (see Table 5.1).

5.2 Setup of simulations

We solve the LES equations in a regular domain of size $512^2 \times 128$ m ($33.4^2 \times 8.4$ in normalized units z/z_h) centered at the tower location (x_t, y_t).

5.2.1 The urban canopy dataset

The previously introduced high resolution three dimensional terrain and building digital model (vector format) is rasterized at a horizontal resolution of 0.5 m and rotated by $-24°$(clockwise) in order to have the main street canyon aligned with our coordinate system (x, y, z). The pdf of roofs' height is characterized by a trimodal distribution (see left plot in Fig. 5.1) with modes at $z \approx 4.5$ m (Mo_1), $z \approx 17.5$ m (Mo_2) and $z \approx 22.5$ m (Mo_3). The mean roof's height z_h is 15.3 m and the variance of roofs' height is 6.4 m. The first mode Mo_1 corresponds to one-storey buildings in the backyards (garages, commercial buildings, etc.), the second mode Mo_2 is related to the the main residential (attached) buildings that line streets and enclose courtyards, whereas the third mode Mo_3 is linked to building N.6 in Fig. 3.2, whose large surface has significant impact on the pdf of the surface heights.

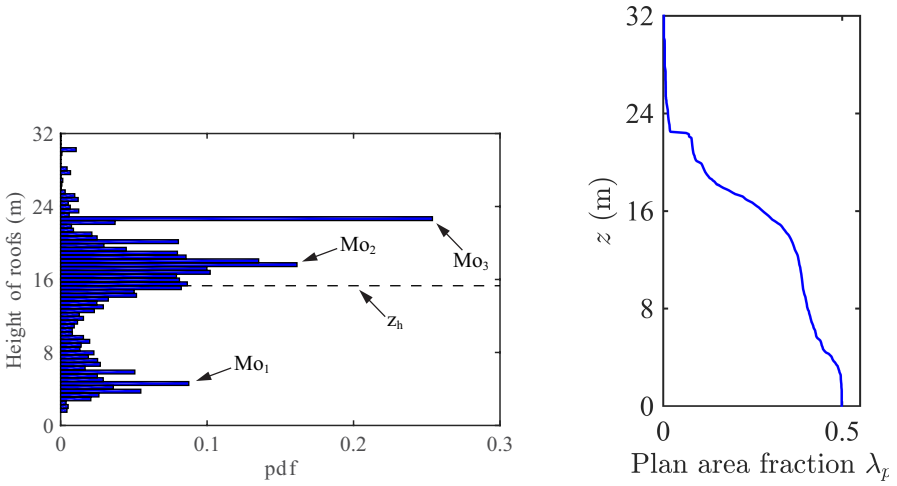

Figure 5.1: Binned pdf of the roofs' height (left) and plan area fraction $\lambda_p(z)$ (right) for the considered surface (512×512 m).

5.2.2 Numerical setup

Table 5.1 summarizes the setup of the current study. We consider two directions of the incoming wind, $\alpha = 66^\circ$ and $\alpha = 156^\circ$, which correspond to an along-canyon and across-canyon regimes respectively. Two subgrid scale models are also considered, the Static Smagorinsky model (Smagorinsky, 1963) and the Lagrangian Scale Dependent Smagorinsky model (Bou-Zeid et al., 2005). We force the flow by imposing a constant pressure gradient $\partial_x p_\infty$, which, together with lateral periodic boundary conditions, defines a friction velocity $u_\tau = \sqrt{(\delta - d)\partial_x \pi_\infty} \approx 1.23$ ms^{-1}, making the system independent from Reynolds number effects (fully rough surface). The pressure forcing in conjunction with lateral periodic boundary conditions are justified given the relatively homogeneous integral morphometric statistics and buildings height in the neighborhood (the main surface transition occurs at ≈ 700 m in the radial direction from the tower location). The hydrodynamic roughness length z_0 is again defined as $z_0 = \Delta/15$, based on a Nyquist-Shannon representation criteria (see Chapter 4

Table 5.1: Geometrical and numerical parameters for the LES runs.

ID	$L_x \times L_y \times L_z$ (m)	$N_x \times N_y \times N_z$	z_0 (m)	α (deg)	SGS model
A	$512 \times 512 \times 160$	$512 \times 512 \times 160$	$\Delta/15$	66	SMAG
B	$512 \times 512 \times 160$	$512 \times 512 \times 160$	$\Delta/15$	156	SMAG
C	$512 \times 512 \times 160$	$512 \times 512 \times 160$	$\Delta/15$	66	LASD
D	$512 \times 512 \times 160$	$512 \times 512 \times 160$	$\Delta/15$	156	LASD

* The computational domains are centered at the tower locations (x_t, y_t).

for a complete justification). To reduce the computational time required to reach a statistically stationary state, the initial velocity field for each simulation is imposed through interpolation from results of a run at coarser resolution (twice as coarse in each coordinate direction). Equations are integrated in time for 480 non-dimensional time units $T = z_h/u_\tau$ (≈ 2 hours in dimensional time) in the coarser grid, before being used as initial condition for the finer grid, where they are further integrated for $250T$. $100T$ are required in order to achieve statistical stationarity in the velocity field and $150T$ are used to compute statistics, which ensures a robust convergence to the expected values for both first and higher order moments. Roughness has a great influence on turbulence up to $z_{RSL}/z_h = \min(1 + D/z_h, 5)$, where D is the separation distance between nearest-neighbour roughness elements (Jimenez, 2004; Raupach and Thom, 1981). Assuming $z_{RSL}/z_h = 5z_h$ and given that the extent of the logarithmic layer is $\approx 0.15\delta$, we cannot expect the ISL to survive. The limited δ/k in the proposed study might be justified by considering that the focus is on the dynamics of the surface layer ($z \lessapprox 5z_h$, where $z_h = 15.3$ m). In these regions turbulence is expected to be strongly affected by the surface details and only in minor part by dynamics of the outer layer.

5.3 Results and discussion

5.3.1 Properties of the instantaneous velocity field

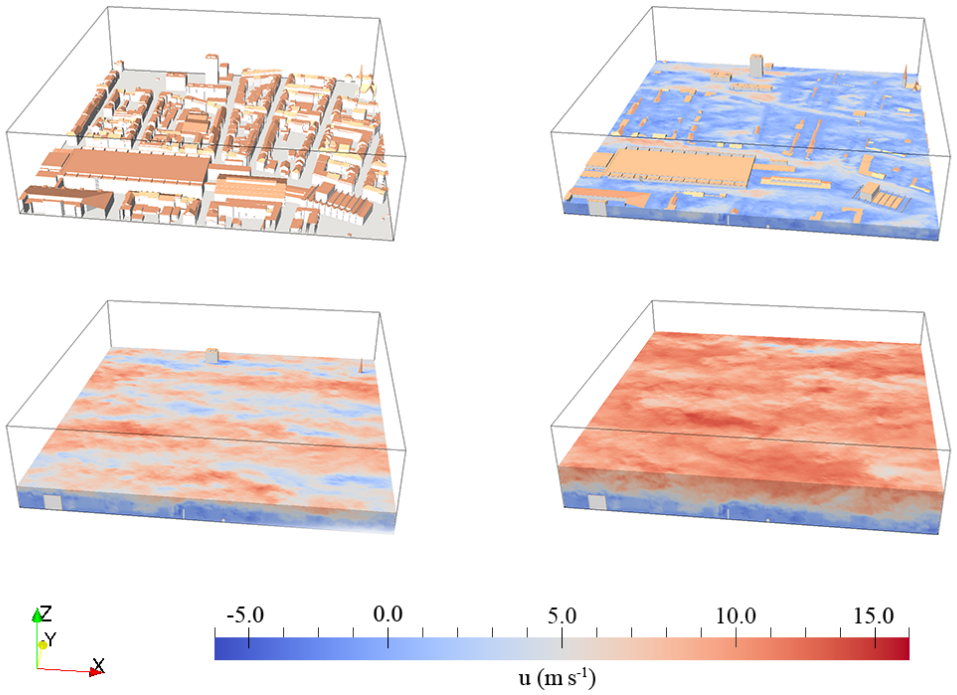

Figure 5.2: From top-left to bottom-right: urban canopy, color contour of (dimensional) stream-wise velocity at the planes $z/z_h = 1$, $z/z_h = 2$, $z/z_h = 4$ for simulation C (across-canyon wind direction). The snapshot represents the flow field at $T^* = 500$ (statistically steady state flow regime). Note that the surface model has been rotated so that the street canyon is perpendicular to the x axis.

To give a qualitative idea of the instantaneous resolved velocity field, a color contour of the stream-wise velocity field from simulation A (across-canyon regime) is displayed in in Fig. 5.2. The flow is characterized by a broad spectra of esplictly resolved length scales, which are heterogeneous in space and strongly depend on the

actual configuration of the buildings.

The relatively high variance characterizing the distribution of roof heights ($\sigma_{z_h}/z_h = 0.42$) causes a transitional behavior between skimming flow and wake interference flow (see definition of flow regimes in Oke (1988)), despite the high value of the plan area fraction covered by buildings (see Fig. 5.1). The lower part of the RSL ($z/z_h \approx 2$) is mainly composed of wake and of non-wake regions (Böhm et al., 2013), whereas as we move further up in the boundary layer the flow organizes itself in a set of relatively high and low-speed streaks.

5.3.2 Mean flow velocity

To facilitate comparison with previous literature, numerical profiles are normalized adopting $u_\tau = \sqrt{\frac{1}{\rho}\frac{\partial \overline{p}_\infty}{\partial x}\delta}$, whereas measured profiles are first rescaled with the ratio between measured and simulated friction velocities at the tower top location $u_\tau(x_t, y_t, z_t)/u_{\tau,tower}(z_t)$, and then normalized with $u_\tau = \sqrt{\frac{1}{\rho}\frac{\partial \overline{p}_\infty}{\partial x}\delta}$, i.e.

$$u^*_{\tau,tower}(z) = \frac{u_\tau(x_t, y_t, z_t)}{u_{\tau,tower}(z_t)} \frac{u_{\tau,tower}(z)}{u_\tau}. \tag{5.1}$$

The rescaling of measured profiles ensures that the measured friction velocity at the tower top location matches with its numerical (local) counterpart. Simulated and measured length scales are normalized with the mean building height of the entire 512×512 m domain ($z_h = 15.3$ m). Throughout the study error bars in tower measurements will denote the standard deviation of sample means, where each sample mean corresponds to 30 min time-average of the considered variable at each z_i^{tower} height (recall the 30 min average blocks are selected by enforcing the constraints defined in Section 2.4), whereas shaded regions in the numerical profiles will denote the standard deviation of the considered variable, at each vertical layer z_i^{LES}, across the considered SGS models (SMAG and LASD) and hydrodynamic roughness lengths

z_0. Note that because we have only 3 blocks of data for $\alpha = 156°$, the standard deviation of the sample means under this approaching wind direction might not be representative of the population standard deviation. Figures 5.3 and 5.4 compare DA and locally-sampled (i.e. extracted from the LES at the tower location) time-averaged $\tilde{u}$ and $\tilde{w}$, against the corresponding mean tower-measured data for the two considered approaching wind directions ($\alpha = 66°$ and $\alpha = 156°$). The locally-sampled

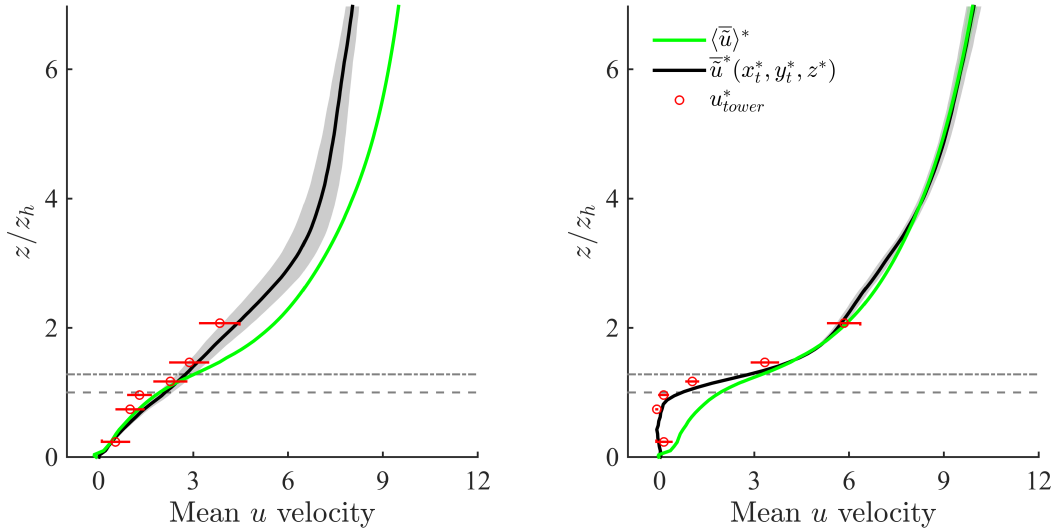

Figure 5.3: DA LES velocity $\langle\overline{\tilde{u}}\rangle^*$ (green) and comparison between time-averaged normalized LES velocity sampled at the tower location $\overline{\tilde{u}}^*(x_t^*, y_t^*, z^*)$ (black) and time-averaged tower-measured velocity $\overline{u}^*_{tower}$ (red dots), for along-canyon wind regime (left) and across-canyon wind regime (right). Horizontal dashed and dot-dashed (grey) lines denote z_h and z_γ respectively. Only the lower 75% of the domain is shown.

time-averaged LES velocity $\overline{\tilde{u}}^*(x_t^*, y_t^*, z^*)$ compares well against $\overline{u}^*_{tower}$ for both wind directions and all heights. Locally sampled and DA LES results are characterized by a modest standard deviation (shaded regions in the LES profiles) throughout the RSL, underlying the limited influence of both z_0 and the SGS closure model in this region

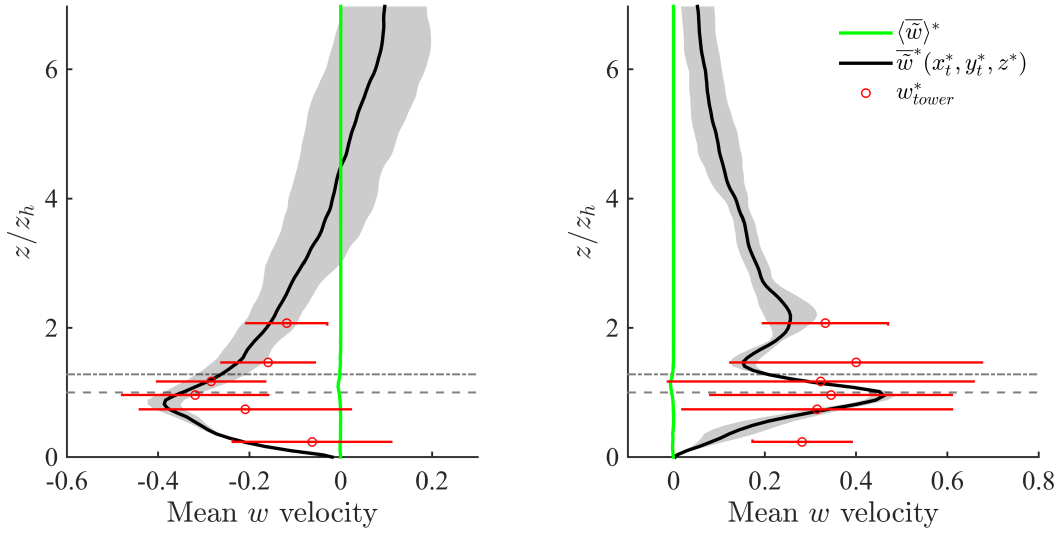

Figure 5.4: DA vertical LES velocity $\langle\overline{\tilde{w}}\rangle^*$ (green) and comparison between time-averaged LES vertical velocity sampled at the tower location $\overline{\tilde{w}}^*(x_t^*, y_t^*, z^*)$ (black) and time-averaged tower-measured velocity $\overline{w}^*_{tower}$ (red dots), for along-canyon wind regime (left) and across-canyon wind regime (right). Horizontal dashed and dot-dashed (grey) lines denote z_h and z_γ respectively. Only the lower 75% of the domain is shown.

of the flow. The relatively larger standard deviation characterizing $\overline{\tilde{u}}^*(x_t^*, y_t^*, z^*)$ in the along-canyon wind regime ($\alpha = 66°$) is mainly due to variation of the dissipation rates across SGS closures. $\overline{\tilde{w}}^*(x_t^*, y_t^*, z^*)$ also compares well against the corresponding $\overline{w}^*_{tower}$ for both along-canyon ($\alpha = 66°$) and across-canyon ($\alpha = 156°$) wind directions, as displayed in Fig. 5.4. Wind approaching from $\alpha = 156°$ leads to convergence of flow in the along-canyon direction, causing a local updraft at the tower location, as apparent from Fig. 5.5. This behavior is in agreement with both tower measurements and wind tunnel results of Feddersen (2005). Further, the lack of a recirculation region for wind approaching from $\alpha = 156°$ (across-canyon regime) is consistent with the study in Kastner-Klein and Rotach (2004), where street canyons characterized by pitched roofs

were connected with no recirculation regions. Wind approaching from $\alpha = 66^\circ$ leads to the formation of long recirculation bubble down-wind of building 8 (see Fig. 3.2), which extends to the tower location (x_t, y_t), hence influencing local statistics. This underlines the strong dependency of the system on the horizontal extension of the computational domain, which should be as large as possible, in particular in the stream-wise direction L_x, to account for upwind buildings and given the strong correlation of the flow in this coordinate direction. Difficulties related to the measurement of vertical velocities justify the observed high variance of $\overline{w}^*_{tower}$ (see Fig. 5.4). DA profiles clearly show an inflection point z_γ for both incoming wind directions, suggesting the presence of a mixing-layer type regime, similar to what observed in flow over a uniform strip canopy (Raupach et al., 1991) and in flow over vegetation canopy (Raupach et al., 1996). Note however that both studies – characterized by roughness of uniform height – identified the inflection point at z_h (i.e. $z_\gamma = z_h$). In the current study, the inflection point z_γ coincides with an effective building height z_e (Christen, 2005b), which can be defined as the averaged surface height, if only buildings higher than 12 m are considered. Introducing an effective building height z_e allows to describe z_γ as a function of the surface height distribution, and is justified given that the majority of low buildings in the backyards, that make up Mo_1 (see Fig. 5.1), do not influence the flow. Further, relating z_γ to z_e allows to recover the limiting behavior $\lim_{\sigma_{z_h} \to 0} z_\gamma = z_e = z_h$ (i.e. when the canopy is characterized by elements of uniform height, the inflection point corresponds to the mean building height). The relatively high location for the inflection point is due to the presence of strong shear layers which separate from the higher roofs and resist penetration by large structures from above (Coceal et al., 2006), thus providing a natural separation layer between high-speed and lower speed regions. Local profiles are very dependent on the specific features of the urban morphometry up to the lower RSL ($1 \lessapprox z/z_h \lessapprox 2$), and are therefore not representative of DA quantities. For the along-canyon regime ($\alpha = 66^\circ$) locally sampled stream-wise velocities ($\widetilde{\overline{u}}(x_t, y_t, z)$) depart from their DA counterparts ($\langle \widetilde{\overline{u}} \rangle$) in the RSL, mainly due to the persistence of

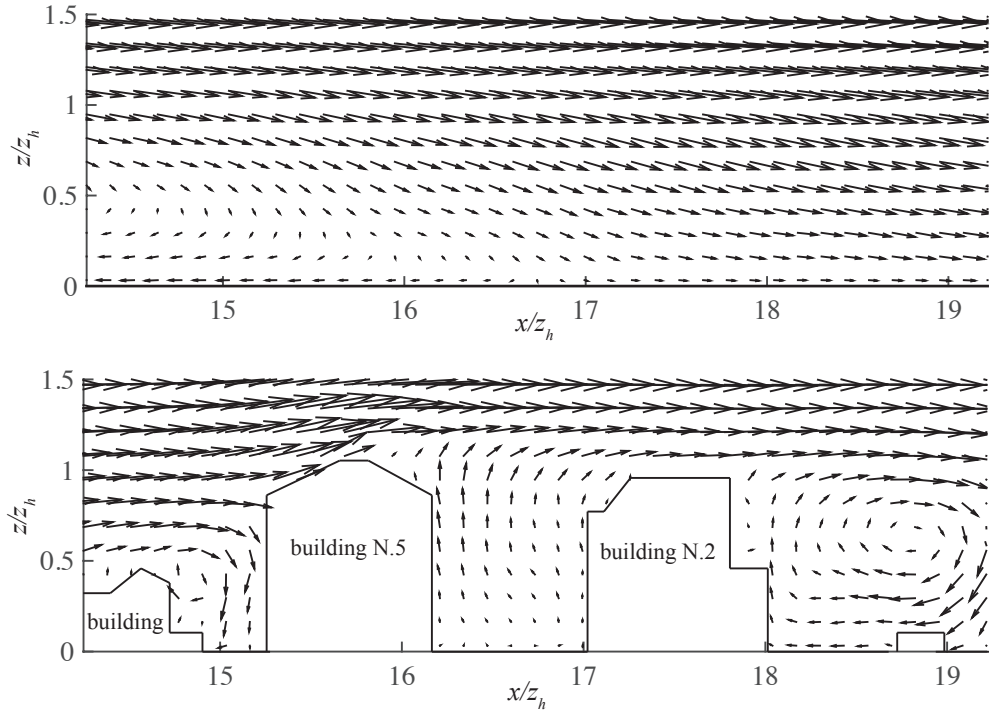

Figure 5.5: Vector plots of the time-averaged velocity field in the $y^* = 16.73$ plane (passing through the tower location) for simulation A (top), corresponding to wind in the along-canyon direction ($\alpha = 66^\circ$), and for simulation C (bottom), corresponding to an across-canyon wind direction ($\alpha = 156^\circ$). The profile tower is located at $x^* = 16.73$ in both plots. Buildings are labeled as in Fig. 3.2 Vectors are generated on a coarser grid (2Δ) for the sake of visualization.

an elongated low speed streak in the RSL, which is locked at the canyon location. This might partly favored by the modest vertical and horizontal extension of the computational domain, which does not allow a full representation of such large scale structures. However, a similar behavior was observed in preliminary tests of flow over a larger domain size $(1536 \times 1536 \times 512$ m) (not shown), which suggests that locking of high and low speed streaks between high-rise buildings is a typical feature of RSL turbulence, and promotes the use of a local scaling approach to collapse profiles in the RSL.

5.3.3 Momentum fluxes

Applying the intrinsic DA operator to the LES momentum conservation equation (Eq. 3.1) results in

$$\frac{1}{\rho}\frac{\partial\langle\overline{\tilde{p}}_{\infty}\rangle}{\partial x} = -\frac{1}{\lambda_p(z)}\frac{\partial}{\partial z}\left[\lambda_p(z)(\langle\overline{\tilde{u}'\tilde{w}'}\rangle + \langle\overline{\tilde{u}}''\overline{\tilde{w}}''\rangle + \langle\overline{\tau}_{xz}^{SGS}\rangle)\right] - \frac{1}{\rho}\left\langle\frac{\partial\overline{\tilde{p}}''}{\partial x}\right\rangle \qquad (5.2)$$

where $\langle\overline{\tilde{u}'\tilde{w}'}\rangle$ is the DA turbulent momentum flux, $\langle\overline{\tilde{u}}''\overline{\tilde{w}}''\rangle$ is the so-called dispersive momentum flux, $\langle\overline{\tau}_{xz}^{SGS}\rangle$ is the subgrid-scale contribution to the momentum flux, and $\frac{1}{\rho}\left\langle\frac{\partial\overline{\tilde{p}}''}{\partial x}\right\rangle$ is the kinematic pressure drag, which performs work against the imposed pressure gradient from the wall $(z=0)$ up to the height of the tallest building $(z_{h_{max}})$. In the considered canopy, buildings occupy a significant fraction of the total volume, thus causing a reduction of the outdoor air volume with depth; this is taken into account through the introduction of the plan area fraction $\lambda_p(z)$ parameter in the intrinsic averaging operation, defined as the fraction of space occupied by fluid in a given horizontal plane, and displayed in Fig. 5.1. To derive Eq. 5.2 we have used the averaging theorem (Whitaker, 1969), which allows to express the DA of a spatial

derivative as the spatial derivative of the DA for a given quantity, i.e.

$$\left\langle \frac{\partial \overline{\theta}}{\partial x_i} \right\rangle = \frac{1}{\lambda_p(z)} \frac{\partial \lambda_p(z) \langle \overline{\theta} \rangle}{\partial x_i} - \frac{1}{A_f} \int_{\partial A_f} \overline{\theta}(x,y,z) n_i dl, \tag{5.3}$$

where θ is any non spatially averaged function, dl is an arc element of the curve ∂A_f, and A_f is a multiply-connected domain, namely the intersection of the constant elevation z plane with the solid interface (the buildings). Integrating Eq. 5.2 analytically in the interval $z \in (z_{h_{max}}, \delta]$, results in

$$\frac{1}{\rho} \frac{d\langle \overline{\tilde{p}}_\infty \rangle}{dx} (\delta - z) = \langle \overline{\tilde{u}' \tilde{w}'} \rangle (z) + \langle \overline{\tilde{u}}'' \overline{\tilde{w}}'' \rangle (z) + \langle \overline{\tau}_{xz}^{SGS} \rangle (z) = \langle \overline{T}_{xz} \rangle (z) \tag{5.4}$$

Eq. 5.4 states that the drag that the flow exerts against the imposed pressure gradient varies linearly with height. This statement does not hold in the interfacial layer, where it is not possible to integrate Eq. 5.2 analytically:

$$\frac{1}{\rho} \frac{d\langle \overline{\tilde{p}}_\infty \rangle}{dx} \int_z^{z_{h_{max}}} \lambda_p(z) dz = -\langle \overline{T}_{xz} \rangle (z_{h_{max}}) + \langle \overline{T}_{xz} \rangle (z) - \int_z^{z_{h_{max}}} \frac{\lambda_p(z)}{\rho} \left\langle \frac{\partial \overline{\tilde{p}}''}{\partial x} \right\rangle dz. \tag{5.5}$$

From Eq. 5.5 is clear how the total drag that the surface exerts against the imposed pressure gradient is a function of the $\lambda_p(z)$ parameter in the interfacial layer, and therefore strongly depends on the morphometry of the considered surface. Each term in Eq. 5.5 scales with $u_\tau^2 = \frac{1}{\rho} \frac{\partial \overline{p}_\infty}{\partial x} \delta$, hence DA profiles are normalized adopting u_τ^2, whereas measured momentum fluxes are first rescaled with $u_\tau^2(x_t, y_t, z_t) / u_{\tau,tower}^2(z_t)$, and then also normalized with u_τ^2, i.e.

$$\overline{\tilde{u}_i' \tilde{u}_j'}_{tower}^{*}(z) = \frac{u_\tau^2(x_t, y_t, z_t)}{u_{\tau,tower}^2(z_t)} \frac{\overline{\tilde{u}_i' \tilde{u}_j'}_{tower}(z)}{u_\tau^2}. \tag{5.6}$$

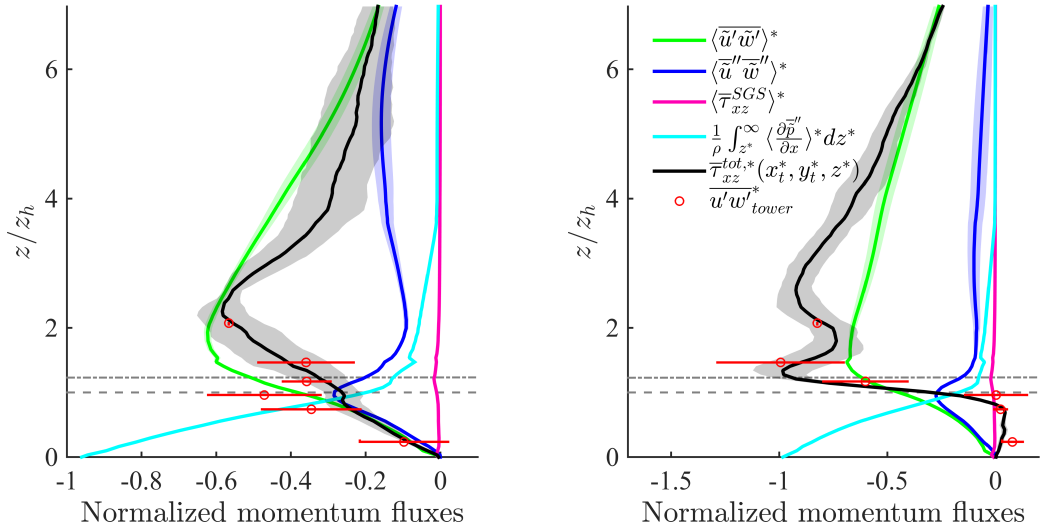

Figure 5.6: Comparison of vertical kinematic fluxes of stream-wise momentum against tower-measured data for the along-canyon (left) and across-canyon (right) wind directions. Notation: DA turbulent momentum fluxes $\langle\widetilde{\overline{u}'\overline{w}'}\rangle^*$, green; dispersive fluxes $\langle\widetilde{\overline{u}}''\widetilde{\overline{w}}''\rangle^*$, blue; DA subgrid fluxes $\langle\overline{\tau}_{xz}\rangle^*$, magenta; DA pressure drag $\frac{1}{\rho}\int_z^\infty\langle\frac{\partial\widetilde{\overline{p}}''}{\partial x}\rangle^* dz$, cyan; time-averaged locally-sampled turbulent + subgrid-scale momentum fluxes $\overline{\tau}_{xz}^{tot,*}(x_t^*, y_t^*, z^*)$, black; tower data, red circles. Horizontal dashed and dot-dashed (grey) lines denote z_h and z_γ respectively. Only the lower 75% of the domain is shown.

Turbulent fluxes

Measured and the corresponding simulated turbulent stresses compare well for the across-canyon regime ($\alpha = 156°$) whereas LES underpredicts the measured turbulent flux in the upper UCL for the along-canyon regime ($\alpha = 66°$). Boundary conditions we could not include in the model, such as cars, trees, temporary structures, etc., might also contribute to the mismatch. From Fig. 5.6 is clear how form drag dominates in the UCL region, whereas in the lower part of the RSL the main sink of momentum is from turbulent and dispersive momentum fluxes ($\widetilde{\overline{u}'\overline{w}'}$ and $\langle\widetilde{\overline{u}}''\widetilde{\overline{w}}''\rangle$ respectively). DA

turbulent momentum fluxes $\langle\widetilde{\tilde{u}'\tilde{w}'}\rangle$ peak above the inflection layer z_γ, presumably due to the advection and turbulent diffusion of wake regions in the vertical – above canopy – direction, as apparent from Fig. 5.7. From Fig. 5.7 is also clear how the taller buildings play a key role in dictating the properties of turbulent stresses, fixing the length scales of wake turbulence, and sheltering smaller buildings. The spatial distribution of selected terms in Fig. 5.7 is representative for the entire domain.

Dispersive fluxes

Dispersive fluxes peak at the average building's height z_h and are of the same sign and approximate magnitude of their DA turbulent counterpart in the UCL. Results from previous studies focusing on flow over arrays of regular and random surface mounted cubes (Coceal et al., 2006; Kono et al., 2010; Martilli and Santiago, 2007; Xie et al., 2008), showed a qualitatively similar trend in the UCL, i.e. dispersive fluxes increase linearly with height up to z_h, but their magnitude was found to be $0.15u_\tau^2$ at most. This is most probably due to the inherent symmetries characterizing idealized geometries. Dispersive fluxes in flow over gravel beds were also found to be significantly smaller than in the current study, with a maximum of about $0.06u_\tau^2$ (Mignot et al., 2009). Further, dispersive stresses are found to gradually decrease with height in the lower RSL, consistent with what reported in studies of flow over urban-like obstacles Xie et al. (2008), and justified by the large variance of the surface height distribution ($\sigma_{z_h} = 0.42z_h$). From Fig. 5.7 it is also clear how dispersive momentum fluxes span a broader range of values when compared against their turbulent counterpart in the RSL, highlighting the strong spatial heterogeneity of such term and the presence of regions in the UCL where strong contributions to the total momentum flux occur (we were however not able to identify any coherent spatial trend).

Pressure drag

Pressure (or form-induced) drag is the main sink of momentum in the UCL. It decreases roughly linearly with height in the UCL, from its surface value $\int_0^\delta \frac{1}{\rho}\frac{\partial\langle\overline{\tilde{p}}''\rangle}{\partial x}dz \approx u_\tau^2$ to roughly the magnitude of DA turbulent stresses at $0.85z_h$. Pressure drag is non-zero up to the height of the tallest building $(z/z_h = 4.18)$, but it is of negligible magnitude down to $z/z_h \approx 1$, when compared against the DA turbulent stresses. As apparent from Fig. 5.7, the largest contribution to the form drag arises in the windward side of buildings, where positive horizontal gradients of pressure occur as the flow approaches the facade. Further, the pressure field is characterized by local minima in the vicinity of the flow separation points for both flat and pitched roofs. In such regions the flow is subjected to strong acceleration.

Subgrid-scale fluxes

SGS fluxes peak at $z_\gamma = z_e$, due to the presence of thin shear layers of fine scale turbulence (see Fig. 5.7), but represent a minor contribution to the total momentum flux in the vertical direction. It is however important to recall that despite the minor role of SGS terms in the momentum balance picture, variations in SGS closure – and thus in the related dissipation rates – can have a strong impact on the resolved scale features. Besides, given that the wall-modeled stresses are also SGS terms, results suggests that when surface roughness is directly resolved (through e.g. an IBM algorithm), the solution for momentum is not sensitive to the wall model. This is a comforting news, given the lack of an universal law of the wall for flows in complex geometries.

5.3.4 Budget of TKE

Within the framework of the DA approach is possible to expand the total filtered kinetic energy (KE) into a temporal and spatial mean (MKE), a wake component (WKE) and

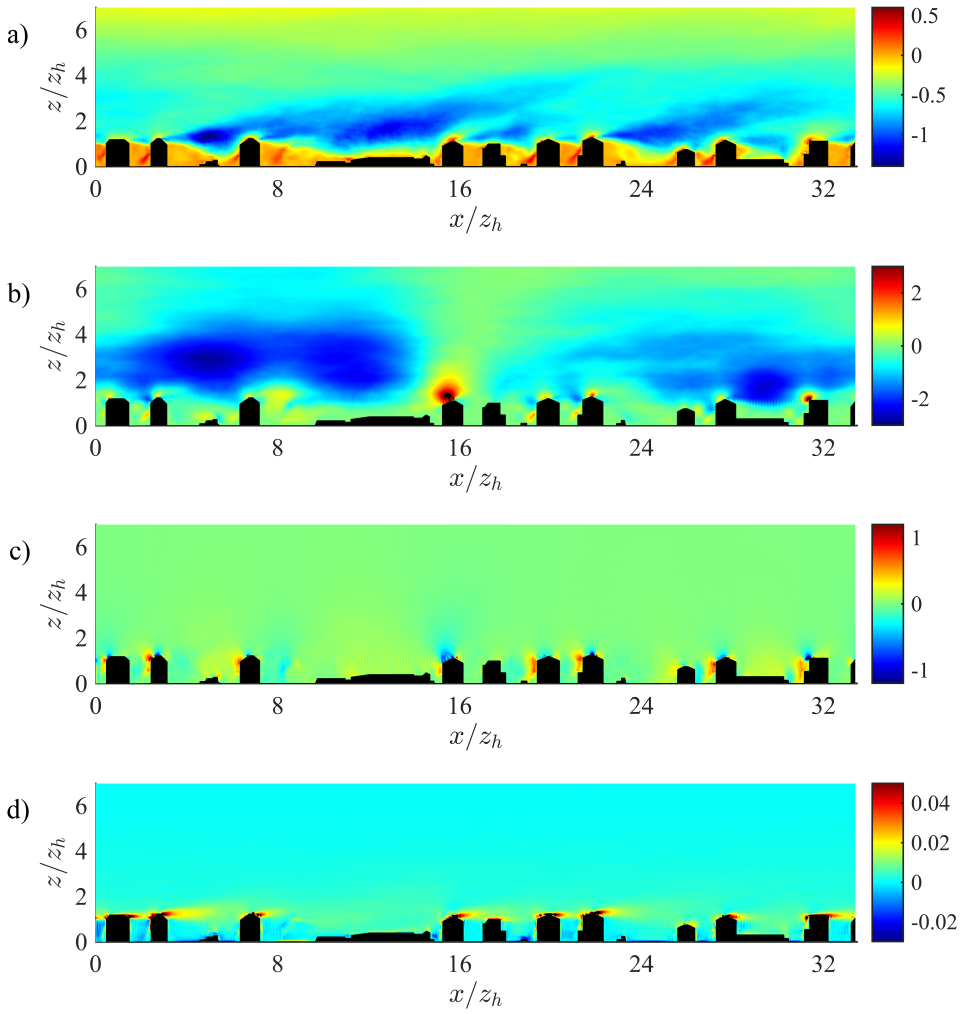

Figure 5.7: Vertical slices intersecting the tower location (plane $y^* = 16.73$) displaying a color contour of turbulent momentum fluxes $\widetilde{\tilde{u}'\tilde{w}'}^*$ (a), of dispersive momentum fluxes $(\overline{\tilde{u}}''\overline{\tilde{w}}'')^*$ (b), of pressure drag $\frac{1}{\rho}(\frac{\partial \overline{\tilde{p}}''}{\partial x})^*$ (c) and of subgrid-scale fluxes $\overline{\tau}^*_{xz}$ (d). Data are from simulation *C* (across-canyon wind direction, $\alpha = 156°$). The lower 75% of the domain is shown.

a turbulent (TKE) component:

$$1/2\langle\tilde{u}_i\tilde{u}_i\rangle = 1/2\left(\langle\overline{\tilde{u}}_i\rangle\langle\overline{\tilde{u}}_i\rangle + \langle\overline{\tilde{u}}_i''\overline{\tilde{u}}_i''\rangle + \langle\overline{\tilde{u}_i'\tilde{u}_i'}\rangle\right), \tag{5.7}$$

Assuming steady state ($\partial(\cdot)/\partial t = 0$) and applying first the time averaging $\overline{(\cdot)}$ and subsequently the intrinsic spatial averaging ($\langle\cdot\rangle$) (Mignot et al., 2008; Nikora et al., 2007) results in the DA TKE budget equation:

$$\begin{aligned}\frac{1}{2}\frac{\partial\langle\overline{\tilde{u}_i'\tilde{u}_i'}\rangle}{\partial t} = &-\langle\overline{\tilde{u}_i'\tilde{w}'}\rangle\frac{\partial\langle\overline{\tilde{u}}_i\rangle}{\partial z} - \left\langle\overline{\tilde{u}_i'\tilde{u}_j'}''\frac{\partial\overline{\tilde{u}}_i''}{\partial x_j}\right\rangle - \langle\overline{\tilde{u}_i'\tilde{w}'}\rangle\left\langle\frac{\partial\overline{\tilde{u}}_i''}{\partial z}\right\rangle \\ &-\frac{1}{\lambda_p}\frac{\partial}{\partial z}\left(\lambda_p(z)\left[\frac{1}{2}\left\langle\overline{\tilde{u}_i'\tilde{u}_i'\tilde{w}'}\right\rangle + \frac{1}{2}\langle\overline{\tilde{w}''\tilde{u}_i'\tilde{u}_i'}''\rangle + \langle\overline{\tilde{\pi}'\tilde{w}'}\rangle\right]\right) \\ &-\frac{1}{\lambda_p}\frac{\partial\lambda_p(z)\langle\overline{\tilde{u}_i'\tau_{iz}'^{SGS}}\rangle}{\partial z} + \langle\overline{\tau_{ij}'^{SGS}\tilde{S}_{ij}'}\rangle,\end{aligned} \tag{5.8}$$

where shear production $P_s = -\overline{\tilde{u}_i'\tilde{w}'}\frac{\partial\overline{\tilde{u}}_i}{\partial z}$, wake production $P_w = -\left\langle\overline{\tilde{u}_i'\tilde{u}_j'}''\frac{\partial\overline{\tilde{u}}_i''}{\partial x_j}\right\rangle$, work of the time-averaged velocity spatial fluctuations against the DA shear stress $P_m = -\langle\overline{\tilde{u}_i'\tilde{w}'}\rangle\left\langle\frac{\partial\overline{\tilde{u}}_i''}{\partial z}\right\rangle$, turbulent transport $T_t = -\frac{1}{2\lambda_p}\frac{\partial\lambda_p\langle\overline{\tilde{u}_i'\tilde{u}_i'\tilde{w}'}\rangle}{\partial z}$, transport by dispersive fluxes $T_d = -\frac{1}{2\lambda_p}\frac{\partial\lambda_p\langle\overline{\tilde{w}''\tilde{u}_i'\tilde{u}_i'}''\rangle}{\partial z}$ pressure transport $T_p = -\frac{1}{\lambda_p}\frac{\partial\lambda_p\langle\overline{\tilde{\pi}'\tilde{w}'}\rangle}{\partial z}$, subgrid transport $D = \frac{1}{\lambda_p}\frac{\partial\lambda_p\langle\overline{\tilde{u}_i'\tau_{i3}'^{SGS}}\rangle}{\partial z}$ and subgrid dissipation $\varepsilon = \langle\overline{\tau_{ij}'^{SGS}\tilde{S}_{ij}'}\rangle$. Given that λ_p varies with height, $P_m \neq 0$ (Mignot et al., 2008), and must be accounted for in the TKE budget.

In the current settings we have that MKE is fed in the system through the imposed pressure gradient, MKE then transfers energy to TKE through the classic cascade process, and to WKE at scale z_h due to the work of the imposed pressure gradient against surface drag. Form drag is a sink term for the MKE, but it also subtracts energy from the large shear-generated eddies, short circuiting the normal eddy-cascade process and enhancing the dissipation rate (Raupach and Thom, 1981). In the following we will first describe the vertical structure of TKE and WKE, to then focus on the

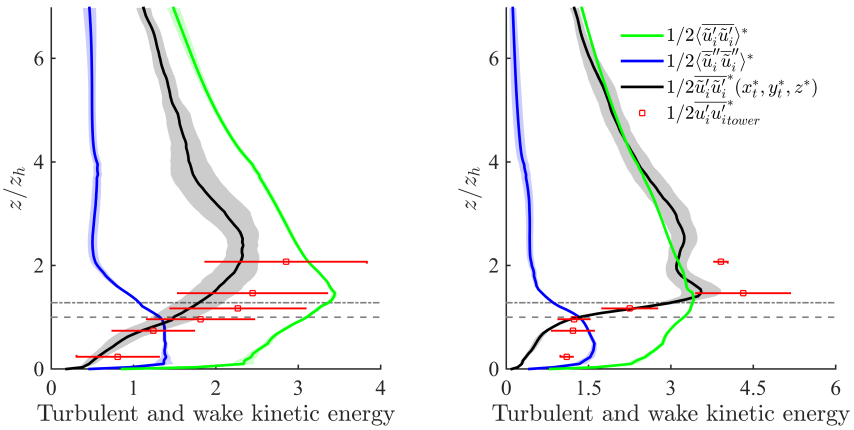

Figure 5.8: Comparison of TKE and WKE against tower-measured data for the along-canyon (left) and across-canyon (right) wind directions. Notation: DA TKE $1/2\langle\widetilde{\overline{u}_i'\overline{u}_i'}\rangle^*$, green; dispersive TKE $1/2\langle\overline{\widetilde{u}_i''\widetilde{u}_i''}\rangle^*$, blue; time-averaged locally-sampled TKE $1/2\overline{\widetilde{u}_i'\widetilde{u}_i'}^*(x_t^*, y_t^*, z^*)$, black; tower data, red circles. Horizontal dashed and dot-dashed (grey) lines denote z_h and z_γ respectively. Only the lower 75% of the domain is shown.

TKE budget terms, for the two considered wind directions. TKE and WKE scale with u_τ^2 and are therefore normalized as previously proposed for momentum fluxes. DA budget profiles are normalized with $u_\tau = \sqrt{\frac{1}{\rho}\frac{\partial \overline{p}_\infty}{\partial x}\delta}$ and z_h (e.g. $\langle P_s\rangle^* = \langle P_s\rangle\frac{z_h}{u_\tau^3}$) whereas measured second order statistics are first rescaled with $u_\tau^3(x_t, y_t, z_t)/u_{\tau,tower}^3$, and then also normalized with u_τ and z_h, e.g.

$$P^*_{s,tower}(z) = \frac{u_\tau^3(x_t, y_t, z_t)}{u_{\tau,tower}^3} P_{s,tower}(z)\frac{z_h}{u_\tau^3}. \tag{5.9}$$

Turbulent and wake kinetic energy

Profiles of turbulent kinetic energy (TKE) and wake kinetic energy (WKE) are shown in Fig. 5.8. Locally sampled time-averaged LES data show relatively good agreement

with measured data for both wind directions. LES slightly under-predict the TKE peak when compared against measured values for the across-canyon wind regime, and this, again, might be in partly due to boundary conditions we could not include in the model. $\langle \frac{1}{2}\overline{\tilde{u}_i'\tilde{u}_i'}\rangle$ peaks at z_γ for the across-canyon wind regime and slightly above z_γ in the along-canyon wind regime, to then decrease linearly with height, consistent with tower measurements for the across-canyon wind regime and in agreement with results from flow over random height cubes (Xie et al., 2008). A peculiar feature of the current study is the remarkable strength of TKE in the UCL, when compared against results from flow over gravel beds (Mignot et al., 2009) or flow over regular/random arrays of cubes (Coceal et al., 2006; Xie et al., 2008), which might be induced by the presence of organized street canyons, which allows the flow to develop significant MKE, which is then cascades into WKE and TKE due to surface drag and the energy cascade process. Further, for both wind directions WKE $\equiv \langle \frac{1}{2}\overline{\tilde{u}}_i''\overline{\tilde{u}}_i''\rangle$ is approximately constant within the UCL $(z \leq z_h)$ and shows a rapid decay in the lower RSL. The relatively large WKE in the RSL for the along-canyon wind regime is due to locking of streaks in between high-rise structures in the RSL.

Table 5.2: Percentage contribution of production, dissipation and transport terms to the total source and sink rate of TKE for the considered layers. Production = $P_s + P_w + P_m$, Transport = $T_t + T_d + T_p + D$.

layer	Production	ε	Transport
UCL $(0 < z < z_h)$	60% $(+)^*$	100% $(-)^*$	40% $(+)$
upper RSL $(z_h < z < 5z_h)$	100% $(+)$	88% $(-)$	12% $(-)$
ISL $(z > 5z_h)$	95% $(+)$	100% $(-)$	5% $(+)$

* (+) denotes a source of TKE, (-) denotes a sink of TKE.

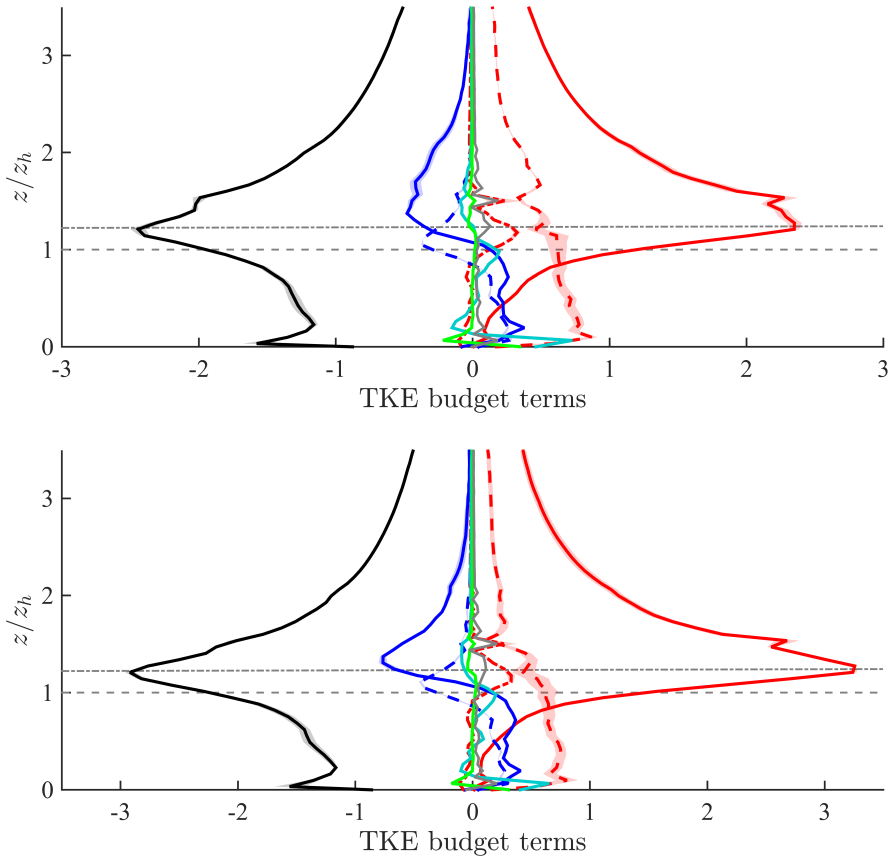

Figure 5.9: DA TKE budget terms for the along-canyon $\alpha = 66^\circ$ (top) and across-canyon $\alpha = 156^\circ$ (bottom) wind directions. Notation: turbulent shear production $\langle P_s \rangle^*$, solid red line; wake production $\langle P_w \rangle^*$, dashed red line; form-induced production $\langle P_m \rangle^*$, dot-dashed red line; dissipation $\langle \varepsilon \rangle^*$, black; turbulent transport $\langle T_t \rangle^*$, solid green line; dispersive transport $\langle T_d \rangle^*$, dashed green line; pressure transport $\langle T_p \rangle^*$, magenta; subgrid transport $\langle D \rangle^*$, blue; residual, grey. Horizontal dashed and dot-dashed (grey) lines denote z_h and z_γ respectively. Only the lower 33% of the domain is shown.

Production terms

Fig. 5.10 compares time-averaged LES profiles, sampled at the tower location, and measured values of shear production. LES results show a remarkable match against measured data, in particular for the across-canyon regime, where the peak in $\langle P_s \rangle$ is well represented. Fig. 5.9 shows that, for both approaching wind angles, DA turbulent shear production $\langle P_s \rangle$ peaks exactly at the inflection point $z_\gamma = 1.28 z_h$. This location is connected with the presence of thin shear layers that separate from the highest buildings, and are advected and diffuse downstream, as displayed in Fig. 5.12. Results are in agreement with findings from studies of flow over a uniform strip canopy (Raupach et al., 1991), where the inflection layer was located at the mean building height, i.e. $z_\gamma = z_h$, and is also in qualitative agreement with results from over canopies of bluff elements (Böhm et al., 2013), which predicted a peak of $\langle P_s \rangle$ at $z_\gamma = 0.86 z_h$. $\langle P_s \rangle$ decreases rapidly from its peak location to approximately zero at the wall, indicating a relatively calm zone in the lower UCL. A second maxima is found in the $\langle P_s \rangle$ profile, at roughly the height of the third mode $\mathrm{Mo}_3 = 22.5$ m of the pdf of buildings' height (see Fig. 5.1), which can be regarded as a very specific feature of the current setup, linked to the shear layers separating from Building N. 6 in Fig. 3.2. $\langle P_w \rangle$ is the production rate of turbulent kinetic energy in the wakes of roughness elements by the interaction of local turbulent stresses and time-averaged strains; in the lower UCL it is approximately constant, positive (WKE converts to TKE) of magnitude $\langle P_w \rangle^* \approx u_\tau^3 / z_h$. $\langle P_w \rangle$ accounts for over 50% the total production rate of TKE in the UCL, and is therefore non-negligible. A previous study of flow over uniform strip canopy (Raupach et al., 1991) found $\langle P_w \rangle$ to increase linearly in the canopy, reach a maxima $\langle P_w \rangle \approx \langle P_s \rangle$ at $z_h = z_\gamma$, and rapidly decrease to zero in the lower RSL. In experimental and numerical studies of flow over gravel beds (Mignot et al., 2009; Yuan and Piomelli, 2014) the magnitude of $\langle P_w \rangle$ was found to be less than 5% of $\langle P_s \rangle$ (based however on a superficial averaging). $\langle P_w \rangle$ thus seems to strongly vary as a function of the roughness properties. Our results suggests that in flows over realistic urban canopies the presence of street

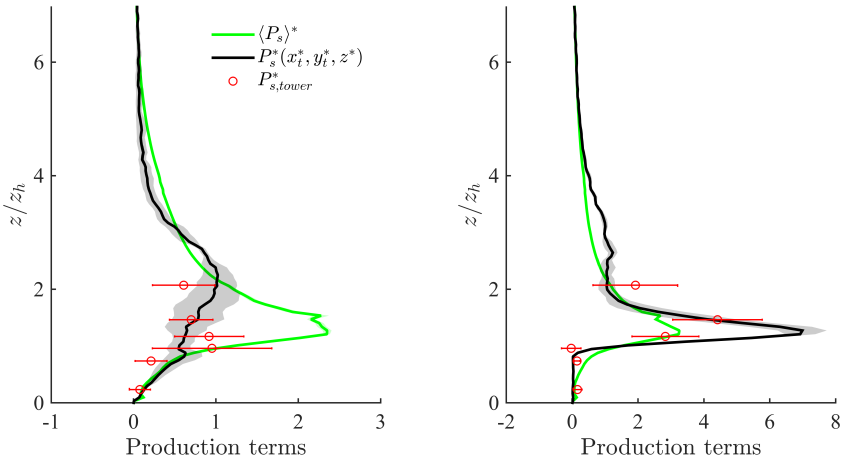

Figure 5.10: TKE production terms for the along-canyon $\alpha = 66°$ (left figure) and across-canyon $\alpha = 156°$ (right figure) wind directions. Notation: DA turbulent production $\langle P_s \rangle^*$, green; locally-sampled time-averaged production $P_s^*(x_t^*, y_t^*, z^*)$, black; turbulent production from tower measurements, red circles. Only the lower 75% of the domain is shown.

canyons aligned with the mean flow, and of variable building geometry tends to increase $\langle P_w \rangle$ in the lower UCL ($z^* \lessapprox 0.5$), when compared to results of flow over strip canopy (Raupach et al., 1991). The additional form-induced production term $\langle P_m \rangle$ is non-zero only in the vicinity of the inflection layer z_γ, where it accounts for 16% the magnitude of $\langle P_s \rangle$. Further, Fig. 5.10 highlights how locally sampled data are not representative of horizontally averaged quantities for $\langle P_s \rangle$. In the across wind regime the tower is located in correspondence of a thin shear layer (see Fig. 5.12), thus overpredicting the peak in P_s, when compared against its horizontally averaged counterpart, whereas in the along-canyon regime the tower is uncapable of properly capture the sharp gradients at z_γ, due to channeling of flow in the Sperrstrasse street canyon, which strongly influences local statistics up to the lower RSL regions.

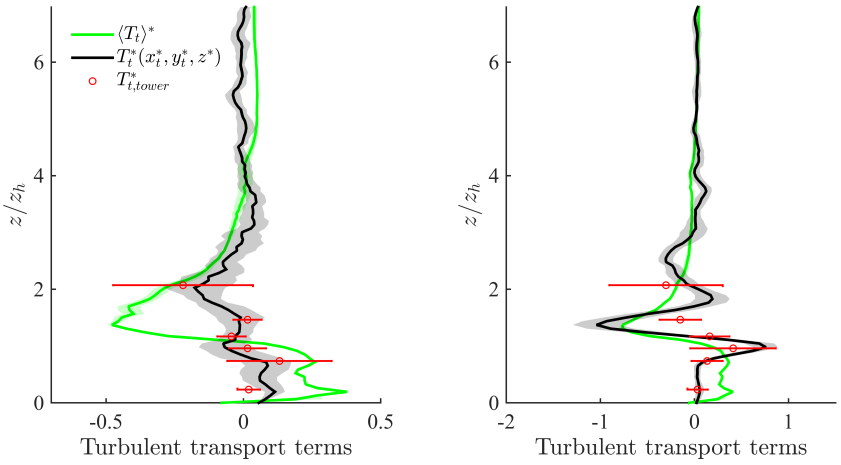

Figure 5.11: Turbulent and dispersive transport terms for the along-canyon $\alpha = 66°$ (left figure) and across-canyon $\alpha = 156°$ (right figure) wind directions. Notation: DA turbulent transport $\langle T_t \rangle^*$, green; locally-sampled time-averaged turbulent transport $T_t^*(x_t^*, y_t^*, z^*)$, black; turbulent transport from tower measurements, red circles. Only the lower 75% of the domain is shown.

Transport terms

Turbulent transport terms are compared against tower measurements in Fig. 5.11. LES shows a similar trend when compared to measured data, but overpredicts $T_t(x_t, y_t, z)$ in the across-canyon regime, suggesting higher resolution might be necessary in order to properly describe the small scale turbulence characterizing the thin shear layers that separate from the roofs of buildings (recall that the current grid stencil is 1 m). DA transport terms are found to be non-negligible throughout the roughness sublayer and profiles are in agreement with data from the same tower, and an additional tower (not shown), operated under a much wider range of stabilities during BUBBLE (Christen et al., 2009). From Fig. 5.9 it is apparent how DA production terms ($\langle P_s \rangle + \langle P_w \rangle + \langle P_m \rangle$) overcome dissipation in the RSL down to z_h, i.e. $z_h \leq z \leq 5z_h$, and DA transport terms are responsible to remove TKE from this layer of high production, and transport it

towards the wall to balance dissipation. In the upper RSL ($z_h < z < 5z_h$) transport terms are thus of negative sign, and contribute to about 12% the total sink rate of TKE (see Table 5.2). They change sign in the UCL, where they are of highest significant, contributing to about 40% the total source rate of TKE (see Table 5.2). $\langle T_w \rangle$ appears as a modulation of $\langle T_t \rangle$, whereas $\langle T_p \rangle$ is significant at z_γ (where it is a sink of TKE) and in the very near wall regions, where it peaks at $\langle T_p \rangle^* = 0.8u_\tau^3/z_h$. Our profiles are in agreement with results of flow over vegetation canopy and with results of flow over gravel beds for the $\langle T_p \rangle$ term, i.e. turbulence in the lowest levels of a canopy is partly induced by pressure perturbations (Shaw and Zhang, 1992; Yuan and Piomelli, 2014). Transport terms peak at the boundaries of the thin shear layers that separate from the top of the buildings, as displayed in Fig. 5.12. Furthermore, is worth noting the modest standard deviation in the computed $\langle T_t \rangle$ terms for both approaching wind directions. This underlies once more the poor sensitivity of the solution with respect to the specific SGS model and to the z_0 parameter, when the roughness is explicitly resolved through an IBM method.

Dissipation and residual terms

DA dissipation $\langle \varepsilon \rangle$ peaks at z_γ, as displayed in Fig. 5.9. This is another peculiar feature of the current study, and is in contrast with results of flow over gravel beds (Mignot et al., 2009; Yuan and Piomelli, 2014), where the peak in dissipation was found to be shifted toward the wall, with respect to the peak in the shear production rate. Further, a strong rate of dissipation characterizes the very near wall regions. This peak is required in order to balance pressure transport of TKE from aloft, again confirming the important role of pressure transport in the vicinity of the wall, in flows over directly resolved building interfaces. Fig. 5.12 underlines how the local dissipation rate spatially resembles the local shear production rate, being significant in the shear layers in the lower RSL. From Fig. 5.12 is also apparent how dissipation is significant in the vicinity of buildings' facades. The relatively modest residual (see Fig.

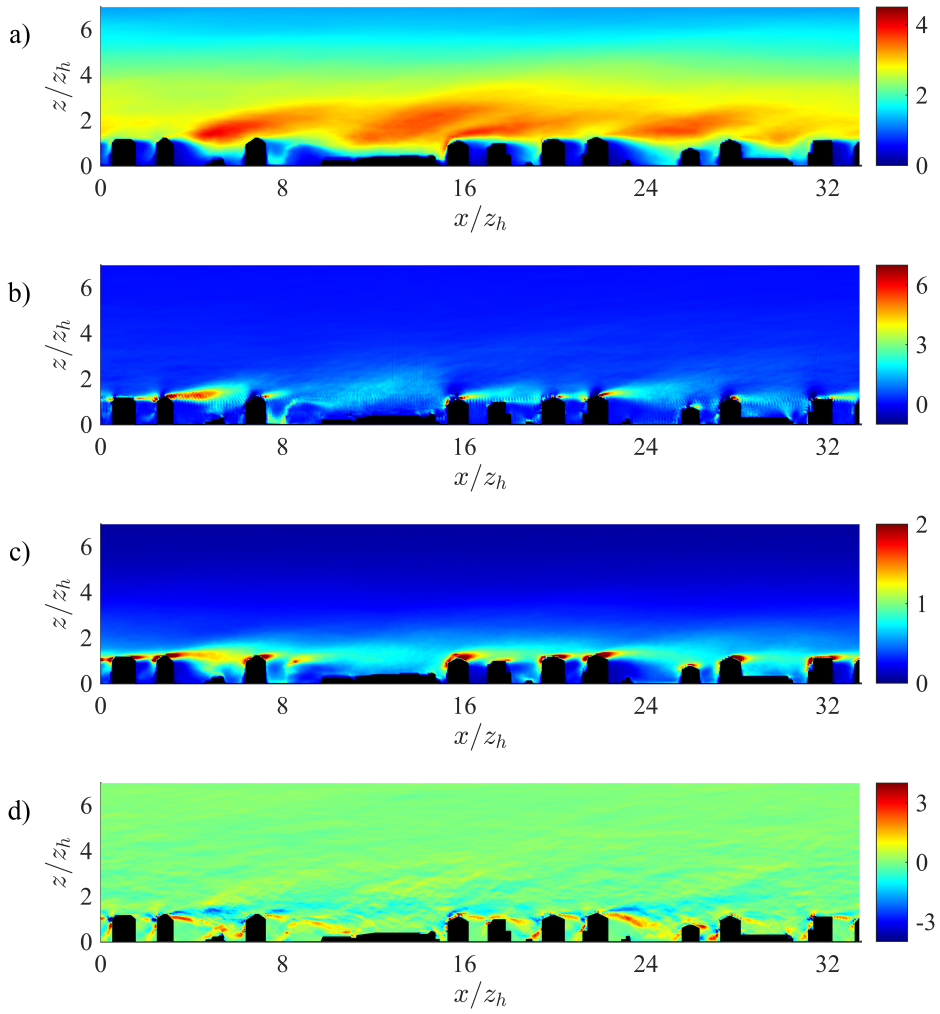

Figure 5.12: Vertical slices intersecting the tower location (plane $y^* = 16.73$) displaying a color contour of TKE* (a), of turbulent shear production P_s^* (b), of dissipation ε^* (c), and total transport $T_{tot}^* = T_t^* + T_d^* + T_p^* + D^*$ (d). Data are from simulation C (across-canyon wind direction, $\alpha = 156^\circ$). The lower 75% of the domain is shown.

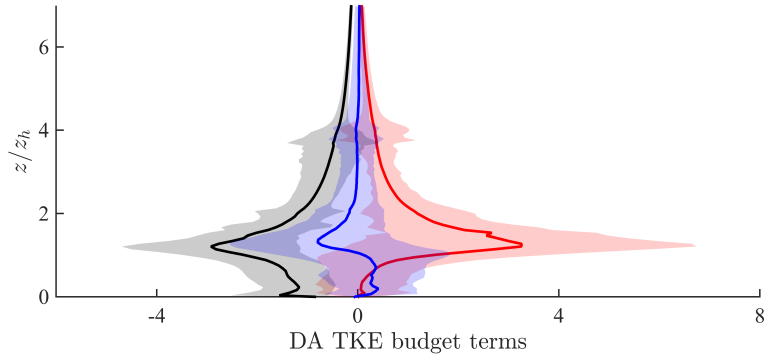

Figure 5.13: Selected DA TKE budget terms for the across-canyon $\alpha = 156^\circ$ wind regime. The displayed standard deviation accounts for the variability related to sampling at different x, y locations in space. Notation: DA turbulent production $\langle P_s^* \rangle$, red; DA dissipation $\langle \varepsilon \rangle^*$, black; DA turbulent transport $\langle T_t \rangle^*$, green. The lower 75% of the domain is shown.

5.9) in the computed TKE budget further validates the proposed results. Is is likely due to interpolation of variables in the near interface regions (which are required to compute certain TKE budget terms), and leads to numerical truncation errors affecting the quality of the computed terms.

Spatial variation of selected TKE budget terms

The standard deviation of selected TKE budget terms, related to sampling at different x, y location in space, is displayed in Fig. 5.13. Locally sampled shear production $\overline{\tilde{P}}_s$ and transport can be either a source or sink of TKE in the UCL, whereas $\overline{\tilde{\varepsilon}}$ – negative by definition – is characterized by a relatively modest spatial standard deviation throughout the RSL, accounting at most for 50% of its magnitude. All the proposed terms are characterized by a high spatial standard deviation at z_γ, underlying the high spatial heterogeneity of such a layer (in contrast with the canonical, homogeneous, mixing layer). Further, a drop in the spatial variance of all considered terms is apparent above

$z/z_h \approx 5$, which can thus be identified as the top of the RSL for the given canopy. These results suggest care should be put when interpreting locally sampled tower measurements, and motivates the use of LES to assess the most appropriate location for the deployment of sensors within urban canopies.

CHAPTER 6

Conclusions and Perspectives

6.1 Concluding remarks

A characterization of mean flow and turbulence over a realistic urban canopy, representing a subset of the city of Basel in Switzerland, has been performed via a series of Large Eddy Simulations (LES) and results have been compared to direct tower measurement from a field campaign. The extent of a representative neighborhood for the area is defined based on the convergence of selected flow statistics (u velocity and shear production rates of TKE $P_s = \langle \overline{\tilde{u}_i' \tilde{u}_j'} \frac{\partial \bar{\tilde{u}}_i}{\partial x_j} \rangle$) as a function of the computational domain. DA and time-averaged locally-sampled (at tower location) profiles of u velocity show modest dependence on the domain size in the RSL ($0 \lessapprox z/z_h \lessapprox 5$), whereas DA P_{tot} profiles strongly depend on both its horizontal and vertical extent. The minimum neighborhood size for the current study is found to be 512×512 m. This allows to obtain representative DA profiles of P_{tot} and to collapse time-averaged

profiles of $\overline{P_s}$, sampled at the tower location. First and higher order statistics compare well against tower measurements, confirming LES in conjunction with IBM a valuable tool for the study of flow and dispersion over realistic urban surfaces. DA numerical profiles are not sensitive to variations in both the SGS model and the z_0 parameter, given that form-drag represents a significant percentage of the total surface drag, and it is explicitly resolved through the immersed boundary method. DA u velocity profiles are characterized by an inflection point z_γ, located above the mean building height z_h, highlighting the presence of a mixing-layer type regime. DA Reynolds fluxes and DA TKE peak above z_γ, in agreement with results from studies of flow over synthetic urban-like surfaces. TKE is significant the UCL, when compared against results of flow over gravel beds and over regular / random arrays of cubes, mainly due to the presence of flow-aligned street canyons, open areas and a variable building height, which strongly increase the strength of both MKE and TKE in such regions. Further, dispersive momentum fluxes and dispersive TKE are found to be non-negligible in the UCL, and of the same magnitude of their Reynolds counterparts. Turbulent kinetic energy (TKE) in the UCL is primarily produced at z_γ by shear, and is transported down into the cavities of the urban canopy (street canyons, backyards) by turbulent and dispersive transport terms, which share similar magnitudes. Transport terms are non-negligible throughout the RSL. They are of negative sign and contribute to about 12% the total variation rate of TKE in the upper RSL ($z_h < z < 5z_h$), whereas they are of highest significance in the UCL ($0 < z < z_h$), where they are of positive sign and contribute to about 40% the local variation rate of TKE. Wake production is roughly constant up to z_γ and of non-negligible magnitude ($\langle P_w \rangle^* \approx u_\tau^3/z_h$), contributing up to 50% the total TKE production rate in the UCL. Further, pressure transport is found to be a significant source of TKE in the near wall regions, in agreement with previous findings in flow over vegetation canopy and flow over gravel beds. From our results it is also apparent how tower measurements cannot be used to quantify all terms in a horizontally-averaged view: the non-measurable dispersive terms are important in a

real canopy and should therefore be considered in future UCPs.

6.2 Further research directions

The proposed work can be extended in multiple directions and we believe represents a useful reference and starting point for further research. In the specific we point out two research paths for future development:

Numerical resolution requirements. One of the challenging features of the proposed work is represented by the high computational cost of simulations. All runs were performed on a cluster composed of several nodes, taking advantage of MPI communication protocols to reduce the wall-clock time. At the chosen resolution, profiles of first and higher order statistics show a good matching against the corresponding measured quantities. However, it would be useful to show how the solution varies as a function of the grid stencil, and to define what are the resolution requirements, based on the goals of the specific study. The realistic settings and the availability of high-quality multi-point sensor data provide in fact a rich framework for such tests, which could represent a reference for future studies. In this regard, we are currently optimizing the parallelism of our LES and IBM algorithms.

Parameterization for dispersive fluxes. We showed how dispersive momentum fluxes have an impact on the vertical transfer rate of momentum, and should therefore be accounted for in future UPCs. It would be therefore important to use the proposed LES data to develop and test a parameterization for such terms, relating them to some readily measurable quantities (e.g. $\langle \overline{u} \rangle$ or $\langle \overline{u_i' u_j'} \rangle$). It would be also possible and interesting to validate the argumentation of Rotach (1993c), which assumes that an observation at a particular point in space represents a variety of upwind and downwind geometries, due to changing wind direction, and that thus spatial averages can be

approximated by averaging over all wind directions of approaching flow.

Characterizing stability effects on the flow. In the proposed study we considered neutrally stratified flow conditions. However, in urban canopies, sources and sinks of heat are ubiquitous, and contribute significantly to the transport of momentum throughout the RSL. A proper characterization of stability effects on the considered system is therefore desirable, since it would allow to better define the properties of RSL turbulence. Further, the realistic settings and the availability of high-quality multi-point sensor data would allow for a detailed comparison between measured and numerical profiles.

Bibliography

Albertson, J. D. and Parlange, M. B. (1999a). Natural integration of scalar fluxes from complex terrain. *Advances in Water Resources*, 23(3):239–252.

Albertson, J. D. and Parlange, M. B. (1999b). Surface length scales and shear stress: Implications for land-atmosphere interaction over complex terrain. *Water Resources Research*, 35(7):2121–2132.

Albertson, J. D. and Parlange, M. B. (1999c). Surface length scales and shear stress: Implications for land-atmospheric interaction over complex terrain. *Water Resour. Res.*, 35(7):2121–2132.

Barlow, J. (2014). Progress in observing and modelling the urban boundary layer. *Urban Climate (In Press)*, 44.

Barlow, J. F. and Coceal, O. (2009). A review of urban roughness sublayer turbulence. *Report*, (527):1–69.

Belcher, S. E. (2005). Mixing and transport in urban areas. *Philosophical transactions. Series A, Mathematical, physical, and engineering sciences*, 363(1837):2947–2968.

Böhm, M., Finnigan, J. J., Raupach, M. R., and Hughes, D. (2013). Turbulence Structure Within and Above a Canopy of Bluff Elements. *Boundary-Layer Meteorology*, 146(3):393–419.

Bou-Zeid, E. (2004). Large-eddy simulation of neutral atmospheric boundary layer flow over heterogeneous surfaces: Blending height and effective surface roughness. *Water Resources Research*, 40(2):n/a–n/a.

Bou-Zeid, E., Meneveau, C., and Parlange, M. (2005). A scale-dependent Lagrangian dynamic model for large eddy simulation of complex turbulent flows. *Physics of Fluids*, 17(2):1–18.

Britter, R. E. and Hanna, S. R. (2003). FLOW AND DISPERSION IN URBAN AREAS. *Annual Review of Fluid Mechanics*, 35(1):469–496.

Cai, W., Gottlieb, D., and Shu, C.-W. (1989). Essentially nonoscillatory spectral Fourier methods for shock wave calculations. *Mathematics of Computation*, 52(186):389–410.

Canuto, C., Hussaini, M. Y., Quarteroni, A., and Zang, T. A. (2006). *Spectral Methods*. Scientific Computation. Springer Berlin Heidelberg, Berlin, Heidelberg.

Cheng, H. and Castro, I. P. (2002). Near wall flow over urban-like roughness. *Boundary-Layer Meteorology*, 104:229–259.

Cheng, W. C. and Porté-Agel, F. (2013). Evaluation of subgrid-scale models in large-eddy simulation of flow past a two-dimensional block. *International Journal of Heat and Fluid Flow*, 44:301–311.

Chester, S., Meneveau, C., and Parlange, M. B. (2007). Modeling turbulent flow over fractal trees with renormalized numerical simulation. *Journal of Computational Physics*, 225(1):427–448.

Chorin, A. J. (1968). Numerical solution of the Navier-Stokes equations. *Mathematics of Computation*, 22:745–762.

Christen, A. (2005a). *Atmospheric Turbulence and Surface Energy Exchange in Urban Environments*. PhD thesis, University of Basel.

Christen, A. (2005b). *Atmospheric Turbulence and Surface Energy Exchange in Urban Environments*. PhD thesis.

Christen, A., Rotach, M. W., and Vogt, R. (2009). The budget of turbulent kinetic energy in the urban roughness sublayer. *Boundary-Layer Meteorology*, 131(2):193–222.

Christen, A., van Gorsel, E., and Vogt, R. (2007). Coherent structures in urban roughness sublayer turbulence. *International Journal of Climatology*, 27(14):1955–1968.

Coceal, O., Thomas, T. G., Castro, I. P., and Belcher, S. E. (2006). Mean flow and turbulence statistics over groups of urban-like cubical obstacles. *Boundary-Layer Meteorology*, 121:491–519.

Eliasen, E., Machenhauer, B., and Rasmussen, E. (1970). *On a numerical method for integration of the hydrodynamical equations with a spectral representation of the horizontal fields*. Kobenhavns Universitet, Institut for Teoretisk Meteorologi.

Eliasson, I., Offerle, B., Grimmond, C., and Lindqvist, S. (2006). Wind fields and turbulence statistics in an urban street canyon. *Atmospheric Environment*, 40(1):1–16.

Feddersen, B. (2005). Wind tunnel modelling of turbulence and dispersion above tall and highly dense urban roughness. *Diss., Naturwissenschaften, Eidgenössische ...*, (15934).

Finnigan, J. J., Einaudi, F., and Fua, D. (1984). The Interaction between an Internal Gravity Wave and Turbulence in the Stably-Stratified Nocturnal Boundary Layer. *Journal of the Atmospheric Sciences*, 41(16):2409–2436.

Germano, M., Piomelli, U., Moin, P., and Cabot, W. H. (1990). A dynamic subgrid-scale eddy viscosity model. *Physics of Fluids A: Fluid Dynamics*, 3(7):1760.

Greer, J. and Banerjee, S. (1997). Exponentially accurate approximations to piece-wise smooth periodic functions. *Journal of Scientific Computing*, 12(3):253–287.

Grimmond, C. S. B., Blackett, M., Best, M. J., Barlow, J., Baik, J.-J., Belcher, S. E., Bohnenstengel, S. I., Calmet, I., Chen, F., Dandou, A., Fortuniak, K., Gouvea, M. L., Hamdi, R., Hendry, M., Kawai, T., Kawamoto, Y., Kondo, H., Krayenhoff, E. S., Lee, S.-H., Loridan, T., Martilli, A., Masson, V., Miao, S., Oleson, K., Pigeon, G., Porson, A., Ryu, Y.-H., Salamanca, F., Shashua-Bar, L., Steeneveld, G.-J., Tombrou, M., Voogt, J., Young, D., and Zhang, N. (2010). The International Urban Energy Balance Models Comparison Project: First Results from Phase 1. *Journal of Applied Meteorology and Climatology*, 49(6):1268–1292.

Grimmond, C. S. B. and Oke, T. R. (1999). Aerodynamic Properties of Urban Areas Derived from Analysis of Surface Form.

Jimenez, J. (2004). Turbulent Flows Over Rough Walls. *Annual Review of Fluid Mechanics*, 36(1991):173–196.

Kanda, M., Inagaki, A., Miyamoto, T., Gryschka, M., and Raasch, S. (2013). A New Aerodynamic Parametrization for Real Urban Surfaces. *Boundary-Layer Meteorology*, 148(2):357–377.

Kastner-Klein, P. and Rotach, M. W. (2004). Mean flow and turbulence characteristics in an urban roughness sublayer. *Boundary-Layer Meteorology*, 111(1):55–84.

Kim, J. and Moin, P. (1985). Application of a fractional-step method to incompressible Navier-Stokes equations. *Journal of Computational Physics*, 59:308–323.

Kono, T., Tamura, T., and Ashie, Y. (2010). Numerical investigations of mean winds within canopies of regularly arrayed cubical buildings under neutral stability conditions. *Boundary-Layer Meteorology*, 134(1):131–155.

Kravchenko, a. G. and Moin, P. (1997). On the Effect of Numerical Errors in Large Eddy Simulations of Turbulent Flows. *Journal of Computational Physics*, 131:310–322.

Lilly, D. K. (1992). A Proposed Modification of the Germano-Subgrid-Scale Closure Method. *Physics of Fluids a-Fluid Dynamics*, 4(3):633–635.

Lu, H. and Porté-Agel, F. (2010). A modulated gradient model for large-eddy simulation: Application to a neutral atmospheric boundary layer. *Physics of Fluids*, 22(1):1–12.

Lu, H. and Porté-Agel, F. (2013). A modulated gradient model for scalar transport in large-eddy simulation of the atmospheric boundary layer. *Physics of Fluids*, 25(1):015110.

Martilli, A. and Santiago, J. L. (2007). CFD simulation of airflow over a regular array of cubes. Part II: Analysis of spatial average properties. *Boundary-Layer Meteorology*, 122:635–654.

Mason, P. J. and Thomson, D. J. (1992). Stochastic backscatter in large-eddy simulations of boundary layers. *Journal of Fluid Mechanics*, 242(-1):51.

Meneveau, C. and Katz, J. (2000). Scale-Invariance and Turbulence Models for Large Eddy Simulation. *Annual Review of Fluid Mechanics*, 32:1–32.

Meneveau, C. and Lund, T. S. (1994). On the Lagrangian nature of the turbulence energy cascade. *Physics of Fluids*, 6(8):2820.

Meneveau, C., Lund, T. S., and Cabot, W. H. (1996). A Lagrangian dynamic subgrid-scale model of turbulence. *Journal of Fluid Mechanics*, 319:353.

Mignot, E., Barthélemy, E., and Hurther, D. (2008). Turbulent kinetic energy budget in a gravel-bed channel flow. *Acta Geophysica*, 56(3):601–613.

Mignot, E., Barthelemy, E., and Hurther, D. (2009). Double-averaging analysis and local flow characterization of near-bed turbulence in gravel-bed channel flows. *Journal of Fluid Mechanics*, 618:279.

Mittal, R. and Iaccarino, G. (2005). Immersed Boundary Methods. *Annual Review of Fluid Mechanics*, 37(1):239–261.

Mohd-Yusof, J. (1997). Combined immersed-boundary/B-spline methods for simulations of ow in complex geometries. *Annual Research Briefs. NASA Ames Research Center . . .* , pages 317–327.

Monin, A. and Obukhov, A. (1954). Basic laws of turbulent mixing in the surface layer of the atmosphere. *Contrib. Geophys. Inst. Acad. Sci. USSR*, 24(151):163–187.

Nikora, V., Goring, D., McEwan, I., and Griffiths, G. (2001). Spatially Averaged Open-Channel Flow over Rough Bed. *Journal of Hydraulic Engineering*, 127(2):123–133.

Nikora, V., McLean, S., Coleman, S., Pokrajac, D., McEwan, I., Campbell, L., Aberle, J., Clunie, D., and Koll, K. (2007). Double-Averaging Concept for Rough-Bed Open-Channel and Overland Flows: Theoretical Background. *Journal of Hydraulic Engineering*, 133(8):884–895.

Nikuradse, J. (1950). *Laws of Flow in Rough Pipes*, volume 3. VDI-Forschungsheft 361.

Oke, T. (1988). Street design and urban canopy layer climate. *Energy and Buildings*, 11(1-3):103–113.

Orszag, S. a. (1969a). Numerical methods for the simulation of turbulence. *Phys. Fluids*, Suppl. II(12):250–257.

Orszag, S. a. (1969b). Numerical Methods for the Simulation of Turbulence. *Physics of Fluids*, 12(12):II–250.

Orszag, S. a. (1970). Transform Method for the Calculation of Vector-Coupled Sums: Application to the Spectral Form of the Vorticity Equation. *Journal of the Atmospheric Sciences*, 27(6):890–895.

Orszag, S. a. (1980). Spectral methods for problems in complex geometries. *Journal of Computational Physics*, 37(1):70–92.

Orszag, S. A. and Pao, Y.-H. (1975). *Turbulent Diffusion in Environmental Pollution, Proceedings of a Symposium held at Charlottesville*, volume 18 of *Advances in Geophysics*. Elsevier.

Pahlow, M., Parlange, M. B., and Porte-Agel, F. (2001). On Monin-Obukhov similarity theory in the stable atmospheric boundary layer. *Boundary-Layer Meteorology*, Vol. 99:225–248.

Peng, Z. and Sun, J. (2014). Characteristics of the Drag Coefficient in the Roughness Sublayer over a Complex Urban Surface. *Boundary-Layer Meteorology*, 153(3):569–580.

Pope, S. B. (2000). *Turbulent Flows*. Cambridge University Press.

Porté-Agel, F. (2004). A scale-dependent dynamic model for scalar transport in large-eddy simulations of the atmospheric boundary layer. *Boundary-Layer Meteorology*, pages 81–105.

Ramamurthy, P., Pardyjak, E. R., and Klewicki, J. C. (2007). Observations of the Effects of Atmospheric Stability on Turbulence Statistics Deep within an Urban Street Canyon. *Journal of Applied Meteorology and Climatology*, 46(12):2074–2085.

Raupach, M. R., Antonia, R. a., and Rajagopalan, S. (1991). Rough-Wall Turbulent Boundary Layers. *Applied Mechanics Reviews*, 44(1):1.

Raupach, M. R., Finnigan, J. J., and Brunei, Y. (1996). Coherent eddies and turbulence in vegetation canopies: The mixing-layer analogy. *Boundary-Layer Meteorology*, 78:351–382.

Raupach, M. R. and Shaw, R. H. (1982). Averaging procedures for flow within vegetation canopies. *Boundary-Layer Meteorology*, 22(1):79–90.

Raupach, M. R. and Thom, a. S. (1981). Turbulence in and above Plant Canopies. *Annual Review of Fluid Mechanics*, 13(1):97–129.

Rotach, M. W. (1993a). Turbulence close to a rough urban surface part I: Reynolds stress. *Boundary-Layer Meteorology*, 65(1-2):1–28.

Rotach, M. W. (1993b). Turbulence close to a rough urban surface part I: Reynolds stress. *Boundary-Layer Meteorology*, 65(1-2):1–28.

Rotach, M. W. (1993c). Turbulence close to a rough urban surface part I: Reynolds stress. *Boundary-Layer Meteorology*, 65(2):1–28.

Rotach, M. W. (1999). On the influence of the urban roughness sublayer on turbulence and dispersion. *Atmospheric Environment*, 33:4001–4008.

Rotach, M. W., Vogt, R., Bernhofer, C., Batchvarova, E., Christen, A., Clappier, A., Feddersen, B., Gryning, S. E., Martucci, G., Mayer, H., Mitev, V., Oke, T. R., Parlow, E., Richner, H., Roth, M., Roulet, Y. A., Ruffieux, D., Salmond, J. a., Schatzmann, M., and Voogt, J. a. (2005). BUBBLE - An urban boundary layer meteorology project. *Theoretical and Applied Climatology*, 81(3-4):231–261.

Roth, M. (2000). Review of atmospheric turbulence over cities. *Quarterly Journal of the Royal Meteorological Society*, 126(564):941–990.

Shannon, C. E. (1993). Communication in the Presence of Noise [1949]. *Proceedings of the IRE*, pages 160–172.

Shaw, R. H. and Zhang, X. J. (1992). Evidence of pressure-forced turbulent flow in a forest. *Boundary-Layer Meteorology*, 58(3):273–288.

Smagorinsky, J. (1963). General Circulation Experiments With the Primitive Equations. *Monthly Weather Review*, 91:99–164.

Stull, R. B. (1988). *An Introduction to Boundary Layer Meteorology*, volume 13. Springer.

Tseng, Y.-H., Meneveau, C., and Parlange, M. B. (2006). Modeling Flow around Bluff Bodies and Predicting Urban Dispersion Using Large Eddy Simulation. *Environmental Science & Technology*, 40(8):2653–2662.

Whitaker, S. (1969). Advances in Theory of Fluid Motion in Porous Media. *Ind. Eng. Chem.*, 61(29):14–28.

Wilson, N. R. and Shaw, R. H. (1977). A Higher Order Closure Model for Canopy Flow. *Journal of Applied Meteorology*, 16:1197–1205.

Xie, Z. and Castro, I. P. (2006). LES and RANS for turbulent flow over arrays of wall-mounted obstacles. *Flow, Turbulence and Combustion*, 76(3):291–312.

Xie, Z. T., Coceal, O., and Castro, I. P. (2008). Large-Eddy simulation of flows over random urban-like obstacles. *Boundary-Layer Meteorology*, 129(1):1–23.

Yuan, J. and Piomelli, U. (2014). Roughness effects on the Reynolds stress budgets in near-wall turbulence. *Journal of Fluid Mechanics*, 760:R1.